Published OnlineFirst March 29, 2012; DOI: 10.1158/0008-5472.CAN-11-3185

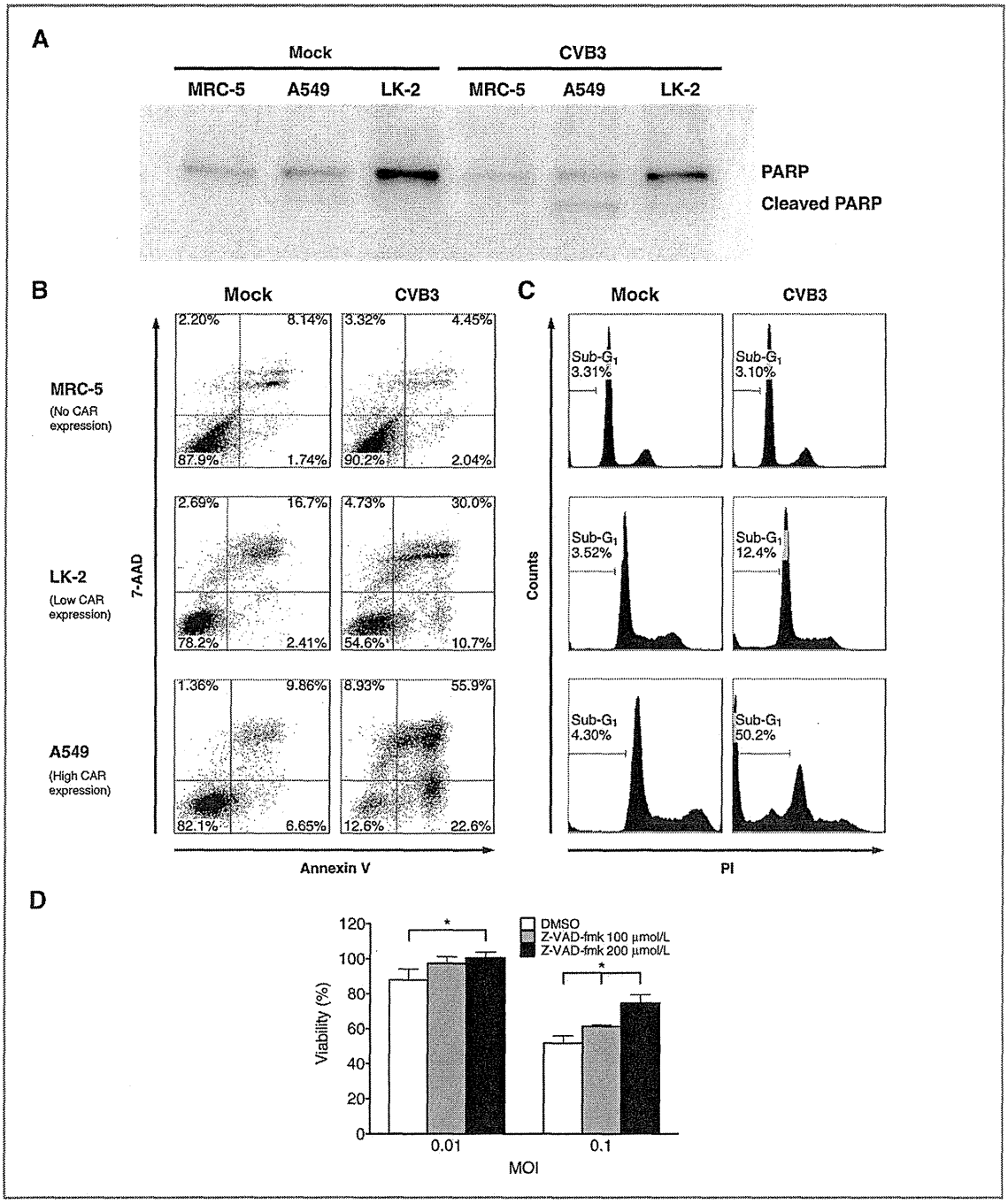

Figure 3. Correlation between caspase-dependent apoptosis and CVB3-mediated cytotoxicity in NSCLC cells. Lung cell lines infected with CVB3 (MOI = 0.1) were analyzed 24 hours later. A, each cellular lysate obtained was subjected to immunoblot analysis. Full-length PARP (116 kDa) and cleaved PARP (85 kDa) are shown. B, early apoptotic population was represented as Annexin V–PE^+/7-AAD^- cells. C, each histogram PI depicts the population of cells in G_1 and G_2–M, and the apoptotic subdiploid peak (sub-G_1). D, cells pretreated with dimethyl sulfoxide (DMSO) or z-VAD-fmk and incubated with mock or CVB3 at indicated MOIs were subjected to MTS cell viability assays. *, $P < 0.05$.

Published OnlineFirst March 29, 2012; DOI: 10.1158/0008-5472.CAN-11-3185

CVB3-inducible apoptosis contributed to CVB3-mediated cytotoxicity against A549 cells, we treated them with the pan-caspase inhibitor, z-VAD-fmk. CVB3-mediated cytotoxicity was slightly but significantly reduced when z-VAD-fmk was added in a dose-dependent manner (Fig. 3D).

Because PI3K/Akt signaling pathways mediate CVB3 replication in human cancer cells (26), we investigated whether CVB3 infection could activate Akt phosphorylation (p-Akt) in A549 cells. CVB3 infection induced substantial p-Akt expression on the Ser-473 residue, peaking at 15 minutes postinfection (Fig. 4A and B), prompting us to examine the effects of pretreatment with LY294002, a specific PI3K inhibitor, or bpV, an inhibitor of PTEN that antagonizes PI3K activity, on p-Akt expression levels in CVB3-treated A549 cells. LY294002 reduced but bpV enhanced the level of p-Akt induced by CVB3 infection (Fig. 4C and D). In addition, LY294002 significantly diminished but bpV significantly augmented CVB3-mediated cytotoxicity against A549 cells at 14 hours after infection in a dose-dependent manner, whereas no cytotoxicity was observed when either of these agents were used in the absence of CVB3 (Fig. 4E and F). To unravel the relationship between p-Akt expression and CVB3 replication, we examined the effects of LY294002 or bpV on release of CVB3 progeny from CVB3-treated A549 cells. The CVB3 titer was significantly reduced when LY294002 was added, whereas it was increased almost 2-fold when bpV was added ($P < 0.05$; Fig. 4G), showing that PI3K/Akt pathway was involved in CVB3 replication. Furthermore, addition of a potent MEK inhibitor PD0325901, which blocks

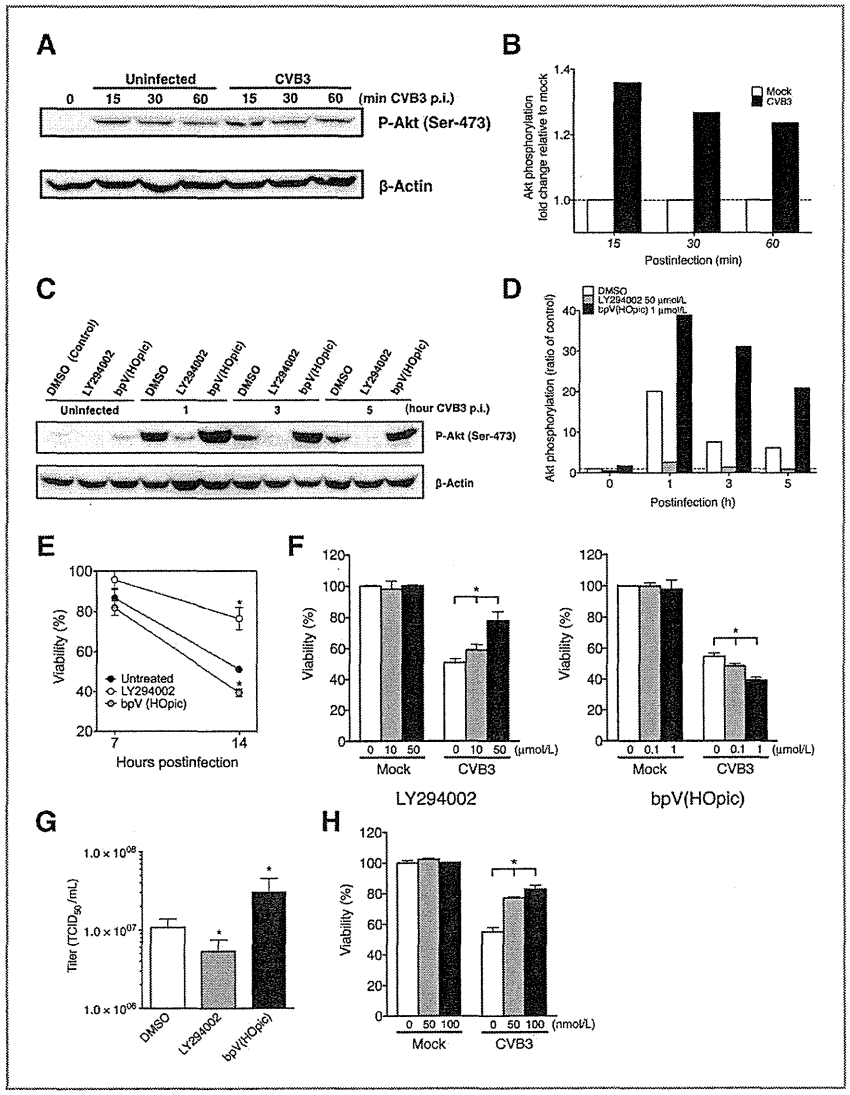

Figure 4. Correlation between 2 survival signaling pathways and CVB3-mediated cytotoxicity and viral replication in human NSCLC cell lines. A549 cells infected with CVB3 (MOI = 0.1) were analyzed. A and B, each cell lysate collected at indicated time points was subjected to Western blotting assay for p-Akt on Ser-473 detection. Results normalized to mock were evaluated by densitometric analysis using Multi Gauge. C and D, p-Akt expression in A549 cells treated with LY294002 or bpV followed by CVB3 infection was determined by Western blotting analysis. E, A549 cells were treated with 50 μmol/L LY294002, 1 μmol/L bpV, or DMSO for 1 hour, infected with CVB3 or Opti-MEM for 1 hour, incubated for 7 or 14 hours, and subjected to MTS cell viability assays. *, $P < 0.05$. F, A549 cells treated as above were incubated for 14 hours at various concentrations of LY294002 or bpV and subjected to MTS cell viability assays. *, $P < 0.05$. G, supernatants from the LY294002- or bpV-treated A549 cells after 14 hours of CVB3 infection were collected and viral titer was determined. *, $P < 0.05$. H, A549 cells were treated with various concentrations of MEK inhibitor PD0325901 or DMSO for 1 hour, followed by CVB3 infection, incubated for 14 hours, and subjected to MTS cell viability assay. *, $P < 0.05$.

Published OnlineFirst March 29, 2012; DOI: 10.1158/0008-5472.CAN-11-3185

phosphorylation of ERK, to CVB3 infection significantly decreased cytotoxicity against A549 cells in a dose-dependent manner, whereas PD0325901 alone did not have any effect (Fig. 4H).

Efficacy studies in nude mice

We next evaluated *in vivo* oncolytic effects of CVB3 and its tolerability in nude mice bearing subcutaneous NSCLC xenografts. A single dose of intratumoral CVB3 administered into A549 xenografts significantly suppressed tumor growth ($P < 0.01$; Fig. 5A). In addition, the survival rate was significantly improved in CVB3-treated mice compared with untreated mice ($P = 0.0008$; Fig. 5B). To evaluate tolerability and dose-dependent oncolytic effects, 5 consecutive doses of CVB3 were intratumorally administered into A549 xenografts. The treatment with CVB3 elicited significant tumor regression in a dose-dependent manner ($P < 0.05$; Fig. 5C), with significantly prolonged survival ($P = 0.0004$). Moreover, half of the CVB3-treated mice achieved complete regression of the tumor (Fig. 5D). Similarly, in the EBC-1 human squamous cell carcinoma xenograft model, intratumoral 5 administrations of CVB3 revealed significant antitumor effects. All CVB3-treated mice achieved complete tumor elimination with a significantly prolonged survival rate (Fig. 5E and F). For H1299 human adenocarcinoma xenograft, similar potent antitumor effects with complete tumor rejection were observed in all of CVB3-treated mice (Supplementary Fig. S3). Notably, none of the mice died of side effects during these treatments.

To further investigate systemic oncolytic effects of CVB3, we used a mouse model with bilaterally preestablished subcutaneous A549 xenografts. Five consecutive CVB3 administrations into the right flank tumors only significantly suppressed the growth of both the CVB3-injected tumor and the distant untreated tumor when compared with untreated mice ($P < 0.05$; Fig. 5G), and displayed a significantly prolonged survival rate ($P = 0.0021$) and no lethality (Fig. 5H). To clarify the mechanism by which CVB3 exerted antitumor effects against the contralateral tumor, we investigated whether the supernatants derived from disrupted untreated tumors or from CVB3-treated tumors had oncolytic activity against A549 cells. The supernatants derived from both CVB3-treated and CVB3-untreated tumors destroyed A549 cells (Fig. 5I), showing that replication-competent CVB3 did exist in untreated contralateral tumors.

Immunologic assays

As preapoptotic exposure to CRT and ATP release and postapoptotic HMGB1 are required for immunogenic cell death induced by chemotherapeutic agents such as anthracyclines and oxaliplatins (18), we examined whether CVB3 infection promoted similar effects on NSCLC cells. CVB3 treatment induced abundant surface exposure of CRT (Fig. 6A) on both A549 and H1299 cells, and active secretion of extracellular ATP was in dose- and time-dependent manner (Fig. 6B). In addition, CVB3 infection resulted in substantial release of HMGB1, another determinant of immunogenicity, from the nuclei of both A549 and H1299 cells into the cytosol (Fig. 6C).

We next evaluated the effects of intratumoral CVB3 administration on tumor-infiltrating immune cells in A549-bearing mice. CVB3 administration recruited significantly greater accumulation of NK cells, granulocytes, macrophages, and DCs into the tumor bed compared with the controls ($P < 0.01$; Fig. 7A and B). The tumor-infiltrating DCs expressed significantly higher levels of the costimulatory molecules CD80, CD86, and the maturation marker CCR7 in CVB3-treated mice compared with untreated mice ($P < 0.05$; Fig. 7C). It has been reported that mobilized CD107a expression, a cytolytic degranulation marker, correlates with NK cell–mediated lytic potential (27), and that granulocytes contribute to the antitumor effect of the oncolytic measles virus (28). We therefore explored the effects of CVB3 treatment on tumor-infiltrating CD107a-harbouring NK cells and granulocytes. A higher density of NK cells as well as granulocytes mobilized CD107a to their cell surface in CVB3-treated mice compared with untreated mice (Fig. 7D). We further investigated the role of endogenous NK cells or granulocytes on the CVB3-mediated antitumor effect by depleting tumor-bearing mice of NK cells or granulocytes. Depletion of either NK cells or granulocytes significantly abrogated the therapeutic effect of CVB3 ($P < 0.05$; Fig. 7E), illustrating their substantial contribution to CVB3-induced antitumor responses.

Discussion

Lung cancer is the world's leading cause of cancer death, resulting in more than 1 million deaths per year worldwide (29). However, standard conventional therapies have produced limited cures, highlighting the need to develop novel therapeutic modalities (30). Here, we successfully identified CVB3 as a useful virotherapeutic agent against NSCLC via large-scale screenings with 28 strains of human enteroviruses (Fig. 1).

Discriminatory mechanisms for selectively targeting cancer cells are a prerequisite for therapeutic oncolytic viruses. CVB3 possessed cancer-specific viral tropism, as evidenced by an extremely low infection of MOI = 0.001 (Fig. 1B). In addition, CVB3-induced cytotoxicity positively correlated with the expression levels of DAF and particularly CAR on NSCLC cells (Fig. 2). CAR is expressed on various histologic types of human lung cancers, but not on normal alveolar epithelial cells (31). DAF counteracts the cytolytic action of the complement system and whose expression is upregulated on the surface of many tumors, seems to be a good target for oncolytic virus (32). These findings form a basis for the use of CVB3 in therapeutic applications for NSCLC patients.

Our results showed a moderate contribution of caspase-mediated apoptosis to CVB3-mediated oncolysis in human NSCLC cells (Fig. 3D). Generally, a wide range of cancers are known to be resistant to apoptosis following chemotherapy (33). Thus, the ability of CVB3 to induce apoptosis is an attractive property for the treatments of refractory NSCLC (34, 35). A role of PI3K/Akt signaling in accelerating CVB3 replication in NSCLC cells was also shown by use of cotreatment with a PTEN inhibitor and CVB3 infection (Fig. 4F and G). Overexpression of p-Akt and loss of PTEN expression in NSCLC

Published OnlineFirst March 29, 2012; DOI: 10.1158/0008-5472.CAN-11-3185

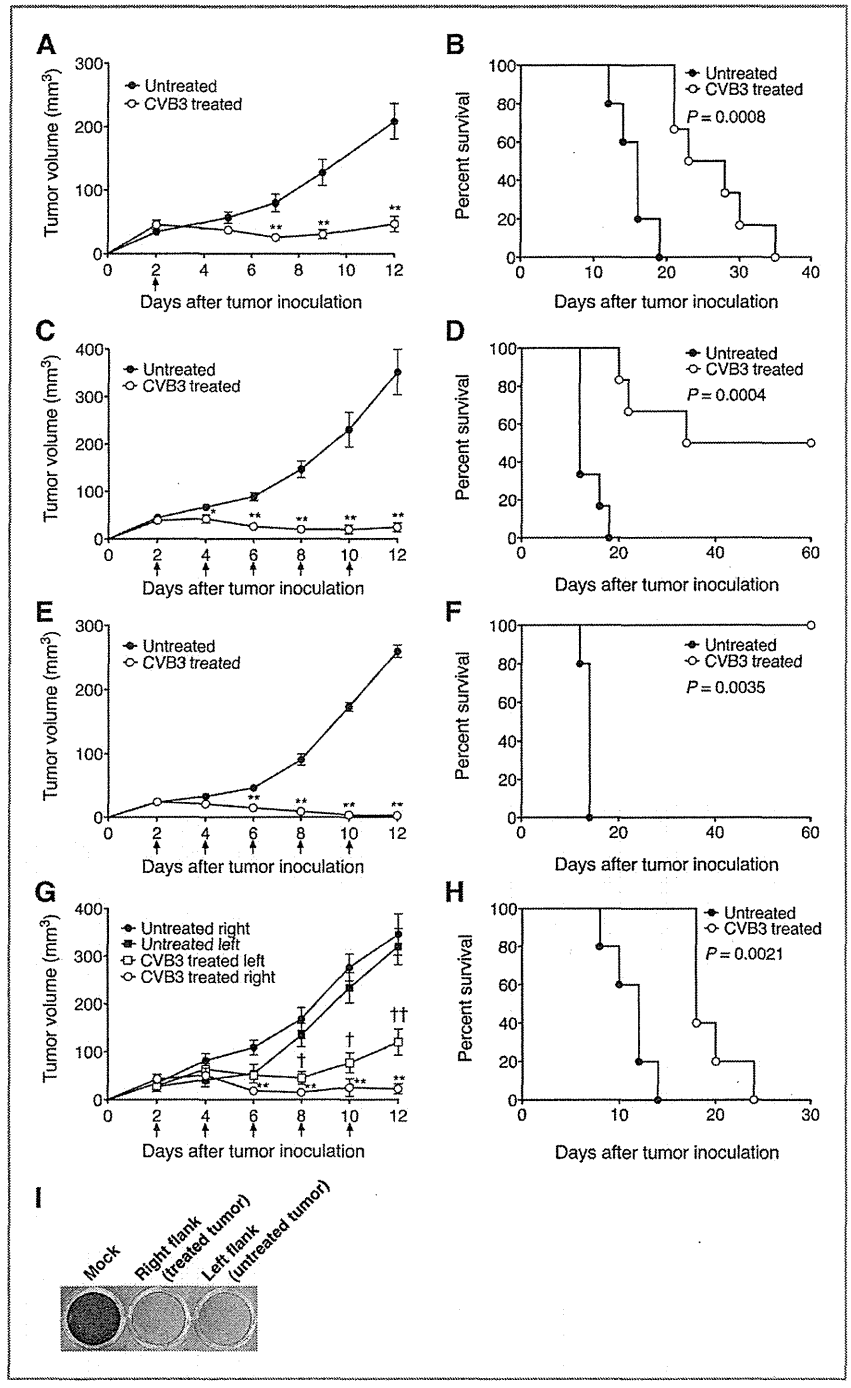

Figure 5. *In vivo* oncolytic effect of intratumoral CVB3 administration on various human NSCLC xenografts. A549 ($n = 5$ or 6; A and C) or EBC-1 ($n = 5$; E) were subcutaneously injected into the right flanks of nude mice. Each mouse received either a single dose (A), or 5 doses (C and E) of CVB3 intratumorally. Tumor volumes are expressed as means ± SEM. *, $P < 0.05$; **, $P < 0.01$. Kaplan–Meier survival analyses are shown for CVB3-treated mice with the single dose (B; $P = 0.0008$) or 5 doses (D; A549, $P = 0.0004$; F; EBC-1, $P = 0.0035$) of the CVB3. G, administration of CVB3 to the right tumor was carried out to the nude mice with bilateral tumors ($n = 5$). *, †, $P < 0.05$; **, ††, $P < 0.01$. Each symbol represents the statistical significance of right (*) and left (†) lateral tumors between untreated and CVB3-treated mice. H, Kaplan–Meier survival analyses of the mice in G are shown ($P = 0.0021$). I, two days after the CVB3 administration, the culture supernatants obtained from bilateral tumors were evaluated for oncolytic activity against cultured A549 cells.

patients was reported to confer poor differentiation, distant metastasis, and poor prognosis (36). In addition, PI3K/Akt pathway–related genes are frequently activated in diverse human cancers including NSCLC tumors (37), and cancer stem cells after systemic chemotherapy (38, 39). These findings suggest that CVB3 treatment may be suitable for NSCLC patients refractory to conventional chemotherapies. In contrast, our finding that PI3K inhibition reduced CVB3

Published OnlineFirst March 29, 2012; DOI: 10.1158/0008-5472.CAN-11-3185

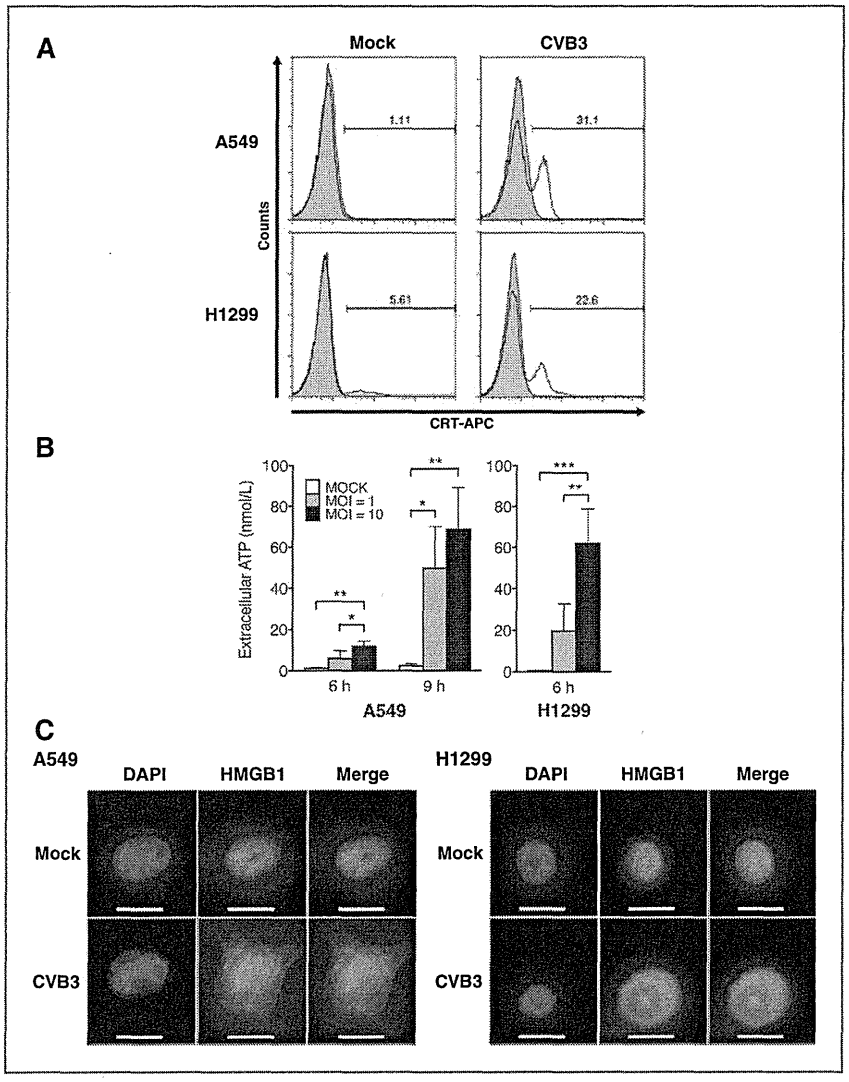

Figure 6. Induced immunogenicity in CVB3-infected NSCLC cells. A, CRT expression on the surface of A549 and H1299 cells was analyzed at 6 hours after CVB3 infection (MOI = 10) by flow cytometric analysis. B, cells were infected with CVB3 at MOI of 1.0 or 10, incubated for 6 or 9 hours, and the concentration of extracellular ATP in the culture medium was measured. Results are shown as means ± SD. *, $P < 0.05$; **, $P < 0.01$; ***, $P < 0.001$. C, immunofluorescence microscopy images of HMGB1 released from nuclei to cytosol in A549 cells infected with CVB3 for 7 hours. Cells were stained with anti-HMGB1 (green) antibody and DAPI (blue), and analyzed by fluorescence microscopy. Scale bars, 10 μm.

production from NSCLC cells raises the possibility that the use of PI3K inhibitors might regulate undesired CVB3 replication. The activity of ERK, the downstream target of MEK in the MEK/ERK survival pathway, was also closely correlated with CVB3-mediated cytotoxicity. Enhanced activation of MEK/ERK has been detected in 34% of 111 primary NSCLC patients with lower survival, but not in normal lung tissue (40, 41), providing further insight into the interplay of CVB3 replication with cellular components to improve antitumor efficacies.

It is noteworthy that intratumoral CVB3 administrations showed significant antitumor effects against A549 adenocarcinoma xenografts resistant to radiotherapy (42) and the EGFR tyrosine kinase inhibitor, gefitinib (43), EBC-1 squamous cell carcinoma (Fig. 5E and F), and H1299 adenocarcinoma xenografts (Supplementary Fig. S3), indicating that CVB3 could be a favorable therapeutic agent for patients with advanced NSCLC refractory to conventional radiotherapies and/or molecular targeted therapies.

Intratumoral CVB3 administration into one of 2 bilateral subcutaneous xenografts elicited significant suppression of growth of the distant uninjected tumors in which oncolytic CVB3 progeny could be detected. This implies that the administered CVB3 replicated, and its progeny circulated via the blood or lymphatic system and infected distant tumors, which is a beneficial for the systemic treatment of metastatic or disseminated tumors.

For toxicity evaluation, we conducted biochemical and histologic assays during CVB3 treatment. CVB3 administration induced moderate hepatic dysfunction (Supplementary Fig. S4A), with no histologic evidence of active hepatitis

Published OnlineFirst March 29, 2012; DOI: 10.1158/0008-5472.CAN-11-3185

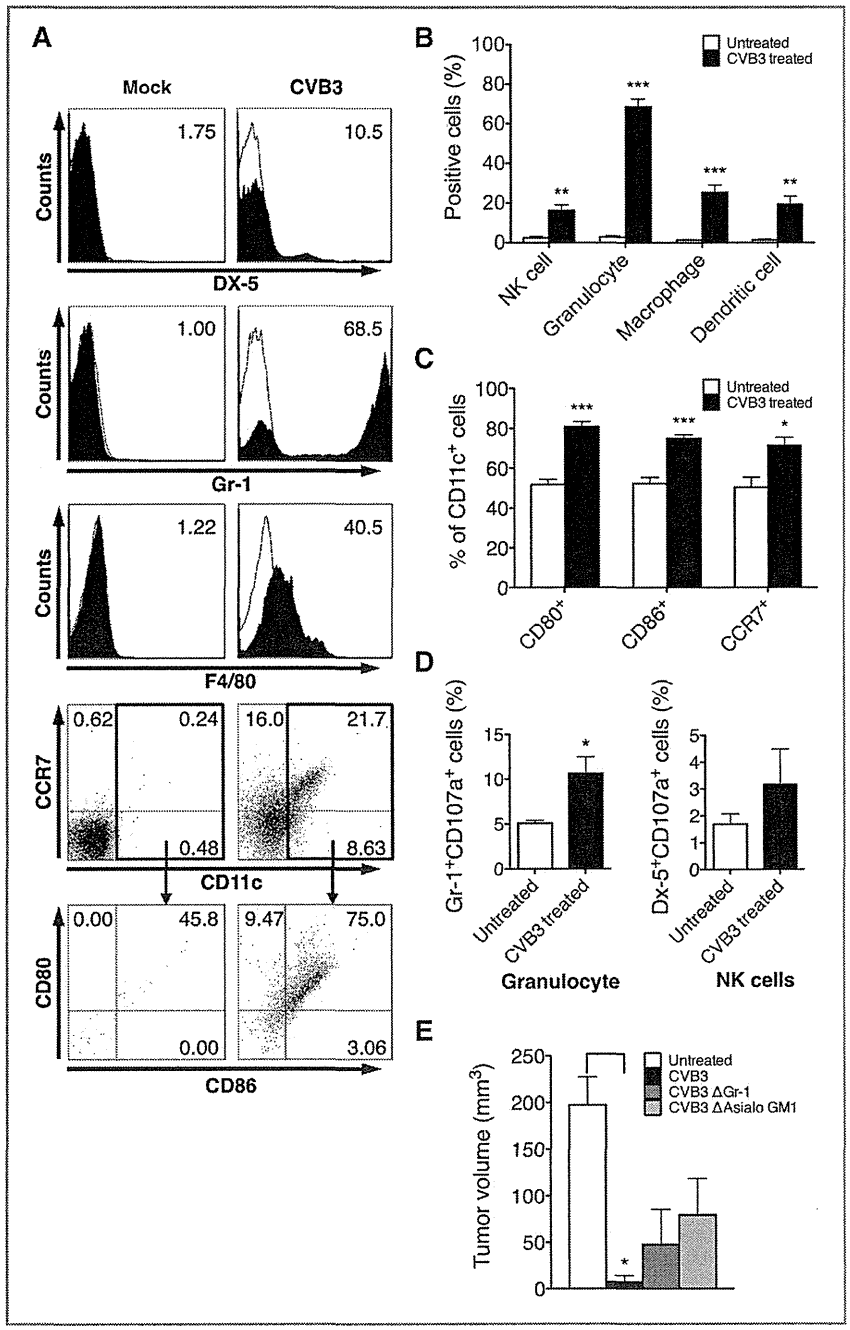

Figure 7. Immunostimulatory effects of intratumoral CVB3 administration on tumor-infiltrating lymphocytes (TIL). TILs obtained on day 2 after intratumoral CVB3 administration were subjected to flow cytometry analysis. A, numbers presented in the histogram reflect the percentage of DX-5$^+$, Gr-1$^+$, F4/80$^+$, and CD11c$^+$ cells relative to the total cell number of TILs (top 3 rows). The numbers presented in 2-dimensional dot plots reflect the percentage of different mature DC subsets relative to the total number of DCs (bottom 2 rows). B, percentages of innate immune subpopulations of NK cells, granulocytes, macrophages, and DCs relative to the total cell count of TILs are shown ($n = 5$). **, $P < 0.01$; ***, $P < 0.001$. C, percentages of 3 different subtypes of mature DCs relative to the total count of DCs are shown. Bar graphs depict the means ± SEM ($n = 5$). *, $P < 0.05$; ***, $P < 0.001$. D, percentages of granulocytes or NK cells expressing CD107a in enriched TILs relative to total TILs are shown. *, $P < 0.05$. E, nude mice ($n = 4$) bearing A549 cells were injected intraperitoneally with anti–Gr-1 antibody on days 1, 4, 7, 10, 13, 16, and 19, or anti-asialo GM1 antibody on days 1, 7, 13, and 19 posttumor challenge. CVB3 virus was injected into the right lateral tumor every other day for a total of 5 doses (5×10^6 $TCID_{50}$/dose). The tumor volumes measured on day 18 are shown ($n = 4$). *, $P < 0.05$.

(Supplementary Fig. S4B). There have been no reports of human hepatitis caused by CVB3 infection. Elevated creatinine kinase was found in the sera of CVB3-treated mice, with histologic evidence of mild myocarditis, but no cytopathic damage in the lungs or kidneys (Supplementary Fig. S4B). Although human CAR mRNA is expressed in the heart (44), CVB3 possibly causes severe myocarditis in infants only (45), suggesting its relatively mild side effects in use for adult patients.

As oncolytic virotherapy is expected to promote inflammatory DAMP within the tumor, which is beneficial for effective antitumor immune responses, it is important to assess

Published OnlineFirst March 29, 2012; DOI: 10.1158/0008-5472.CAN-11-3185

whether oncolytic viruses generate immunogenic cell death (18). CVB3 infection induced these immunogenic changes such as CRT exposure, release of extracellular ATP, and HMGB1 translocation in NSCLC cells (Fig. 6). Upon propagation of oncolytic virus, alterations in the repertoire of immune cells in tumor microenvironment can restore inherent antitumor immunity (46), through inductions of interferons and/or cytokines that activate NK cells and mature DCs (47, 48). Tumor-infiltrating DCs have been shown to be impaired at maturation (49). Media from malignant cells infected with reovirus promoted maturation of DCs (46). Likewise CVB3 may alter the immunologic microenvironment by accumulating diverse mature DCs into tumors (Fig. 7C), probably because the single-stranded RNA genome converts dysfunctional DCs into functional DCs after ligation of retinoic acid–inducible gene-1 (RIG-1)-like receptors (50). Indeed, CVB3 intervention was shown to shape NK cell polarization with antitumor effects, possibly through promoted recruitment of cytolytic $CD107a^+$ NK cells into xenografts (Fig. 7D and E). Contribution of neutrophils to the antitumor effects may be partially due to IFN-β production following CVB3 administration, as IFN-β can instruct neutrophils to possess an antitumor phenotype (51). These immunostimulatory properties of CVB3 on innate immunity may subsequently prime effective generation of adaptive immunity synergizing with direct oncolytic activities. After showing that TC-1 syngeneic mouse NSCLC cells were susceptible to *in vitro* CVB3 infection (Supplementary Fig. S5A), to further evaluate the effects of T cell–mediated cellular immunity on the oncolytic effects of CVB3, we treated immunocompetent mice with TC-1 tumors with a single CVB3 intratumoral administration, which significantly inhibited TC-1 tumor development in a dose-dependent manner ($P < 0.05$; Supplementary Fig. S5B), with significantly prolonged survival (Supplementary Fig. S5C). These findings indicate that T cell–mediated antiviral immunity is not a significant barrier for intratumoral replication of CVB3.

Notably, in all experiments, no mice manifested lethality during CVB3 treatments, highlighting acceptable safety characteristics as an oncolytic agent.

In summary, our large-scale 2-step screening identified CVB3 as a tumor-specific virus, which depends on apoptotic and survival signaling pathways. Furthermore, systemic and immunostimulatory antitumor effects of CVB3 provide an encouraging avenue for future preclinical and clinical development as a promising viral agent for the treatment of NSCLC patients.

Disclosure of Potential Conflicts of Interest

K. Tani: minor stock, Oncolys BioPhama Inc. No potential conflicts were disclosed by the other authors.

Acknowledgments

The authors thank Michiyo Okada, Michiko Ushijima, and Dr. Shinji Okano (Kyushu University) for technical assistance. The authors also thank the technical support from the Research Support Center, Graduate School of Medical Sciences, Kyushu University.

Grant Support

This work was supported by grants from the Ministry of Education, Culture, Sports, Science and Technology (17016053 and 23240133), and the Ministry of Health Labour and Welfare (23080101), Japan.

The costs of publication of this article were defrayed in part by the payment of page charges. This article must therefore be hereby marked *advertisement* in accordance with 18 U.S.C. Section 1734 solely to indicate this fact.

Received September 23, 2011; revised February 24, 2012; accepted March 14, 2012; published OnlineFirst March 29, 2012.

References

1. Russell SJ, Peng KW. Viruses as anticancer drugs. Trends Pharmacol Sci 2007;28:326–33.
2. Aghi M, Martuza RL. Oncolytic viral therapies—the clinical experience. Oncogene 2005;24:7802–16.
3. Park BH, Hwang T, Liu TC, Sze DY, Kim JS, Kwon HC, et al. Use of a targeted oncolytic poxvirus, JX-594, in patients with refractory primary or metastatic liver cancer: a phase I trial. Lancet Oncol 2008;9:533–42.
4. Kumar S, Gao L, Yeagy B, Reid T. Virus combinations and chemotherapy for the treatment of human cancers. Curr Opin Mol Ther 2008;10:371–9.
5. Morton CL, Houghton PJ, Kolb EA, Gorlick R, Reynolds CP, Kang MH, et al. Initial testing of the replication competent Seneca Valley virus (NTX-010) by the pediatric preclinical testing program. Pediatr Blood Cancer 2010;55:295–303.
6. Shafren DR, Sylvester D, Johansson ES, Campbell IG, Barry RD. Oncolysis of human ovarian cancers by echovirus type 1. Int J Cancer 2005;115:320–8.
7. Au GG, Beagley LG, Haley ES, Barry RD, Shafren DR. Oncolysis of malignant human melanoma tumors by Coxsackieviruses A13, A15 and A18. Virol J 2011;8:22.
8. Shafren DR, Au GG, Nguyen T, Newcombe NG, Haley ES, Beagley L, et al. Systemic therapy of malignant human melanoma tumors by a common cold-producing enterovirus, coxsackievirus a21. Clin Cancer Res 2004;10:53–60.
9. Skelding KA, Barry RD, Shafren DR. Enhanced oncolysis mediated by Coxsackievirus A21 in combination with doxorubicin hydrochloride. Invest New Drugs 2012;30:568–81.
10. Feuer R, Mena I, Pagarigan R, Slifka MK, Whitton JL. Cell cycle status affects coxsackievirus replication, persistence, and reactivation *in vitro*. J Virol 2002;76:4430–40.
11. Evans DJ. Reverse genetics of picornaviruses. Adv Virus Res 1999;53:209–28.
12. Michos AG, Syriopoulou VP, Hadjichristodoulou C, Daikos GL, Lagona E, Douridas P, et al. Aseptic meningitis in children: analysis of 506 cases. PLoS One 2007;2:e674.
13. Skelding KA, Barry RD, Shafren DR. Systemic targeting of metastatic human breast tumor xenografts by Coxsackievirus A21. Breast Cancer Res Treat 2009;113:21–30.
14. Kelly EJ, Hadac EM, Greiner S, Russell SJ. Engineering microRNA responsiveness to decrease virus pathogenicity. Nat Med 2008;14:1278–83.
15. Diaz RM, Galivo F, Kottke T, Wongthida P, Qiao J, Thompson J, et al. Oncolytic immunovirotherapy for melanoma using vesicular stomatitis virus. Cancer Res 2007;67:2840–8.
16. Matzinger P. Tolerance, danger, and the extended family. Annu Rev Immunol 1994;12:991–1045.
17. Prestwich RJ, Errington F, Ilett EJ, Morgan RS, Scott KJ, Kottke T, et al. Tumor infection by oncolytic reovirus primes adaptive antitumor immunity. Clin Cancer Res 2008;14:7358–66.
18. Zitvogel L, Kepp O, Senovilla L, Menger L, Chaput N, Kroemer G. Immunogenic tumor cell death for optimal anticancer therapy: the calreticulin exposure pathway. Clin Cancer Res 2010;16:3100–4.
19. Kuninaka S, Yano T, Yokoyama H, Fukuyama Y, Terazaki Y, Uehara T, et al. Direct influences of pro-inflammatory cytokines (IL-1beta, TNF-

Published OnlineFirst March 29, 2012; DOI: 10.1158/0008-5472.CAN-11-3185

alpha, IL-6) on the proliferation and cell-surface antigen expression of cancer cells. Cytokine 2000;12:8–11.
20. Karber G. 50% end-point calculation. Arch Exp Pathol Pharmak 1931;162:480–3.
21. Meng X, Nakamura T, Okazaki T, Inoue H, Takahashi A, Miyamoto S, et al. Enhanced antitumor effects of an engineered measles virus Edmonston strain expressing the wild-type N, P, L genes on human renal cell carcinoma. Mol Ther 2010;18:544–51.
22. Tesniere A, Schlemmer F, Boige V, Kepp O, Martins I, Ghiringhelli F, et al. Immunogenic death of colon cancer cells treated with oxaliplatin. Oncogene 2010;29:482–91.
23. Inoue H, Iga M, Xin M, Asahi S, Nakamura T, Kurita R, et al. TARC and RANTES enhance antitumor immunity induced by the GM-CSF-transduced tumor vaccine in a mouse tumor model. Cancer Immunol Immunother 2008;57:1399–411.
24. Inoue H, Iga M, Nabeta H, Yokoo T, Suehiro Y, Okano S, et al. Non-transmissible Sendai virus encoding granulocyte macrophage colony-stimulating factor is a novel and potent vector system for producing autologous tumor vaccines. Cancer Sci 2008;99:2315–26.
25. Shafren DR, Williams DT, Barry RD. A decay-accelerating factor-binding strain of coxsackievirus B3 requires the coxsackievirus-adenovirus receptor protein to mediate lytic infection of rhabdomyosarcoma cells. J Virol 1997;71:9844–8.
26. Esfandiarei M, Luo H, Yanagawa B, Suarez A, Dabiri D, Zhang J, et al. Protein kinase B/Akt regulates coxsackievirus B3 replication through a mechanism which is not caspase dependent. J Virol 2004;78:4289–98.
27. Alter G, Malenfant JM, Altfeld M. CD107a as a functional marker for the identification of natural killer cell activity. J Immunol Methods 2004;294:15–22.
28. Grote D, Cattaneo R, Fielding AK. Neutrophils contribute to the measles virus-induced antitumor effect: enhancement by granulocyte macrophage colony-stimulating factor expression. Cancer Res 2003; 63:6463–8.
29. Jemal A, Bray F, Center MM, Ferlay J, Ward E, Forman D. Global cancer statistics. CA Cancer J Clin 2011;61:69–90.
30. Fidias P, Novello S. Strategies for prolonged therapy in patients with advanced non-small-cell lung cancer. J Clin Oncol 2010;28:5116–23.
31. Wang Y, Wang S, Bao Y, Ni C, Guan N, Zhao J, et al. Coxsackievirus and adenovirus receptor expression in non-malignant lung tissues and clinical lung cancers. J Mol Histol 2006;37:153–60.
32. Li L, Spendlove I, Morgan J, Durrant LG. CD55 is over-expressed in the tumour environment. Br J Cancer 2001;84:80–6.
33. Dean M, Fojo T, Bates S. Tumour stem cells and drug resistance. Nat Rev Cancer 2005;5:275–84.
34. Carthy CM, Yanagawa B, Luo H, Granville DJ, Yang D, Cheung P, et al. Bcl-2 and Bcl-xL overexpression inhibits cytochrome c release, activation of multiple caspases, and virus release following coxsackievirus B3 infection. Virology 2003;313:147–57.
35. Martin U, Jarasch N, Nestler M, Rassmann A, Munder T, Seitz S, et al. Antiviral effects of pan-caspase inhibitors on the replication of coxsackievirus B3. Apoptosis 2007;12:525–33.
36. Tang JM, He QY, Guo RX, Chang XJ. Phosphorylated Akt overexpression and loss of PTEN expression in non-small cell lung cancer confers poor prognosis. Lung Cancer 2006;51:181–91.
37. Balsara BR, Pei J, Mitsuuchi Y, Page R, Klein-Szanto A, Wang H, et al. Frequent activation of AKT in non-small cell lung carcinomas and preneoplastic bronchial lesions. Carcinogenesis 2004;25:2053–9.
38. Zhou J, Wulfkuhle J, Zhang H, Gu P, Yang Y, Deng J, et al. Activation of the PTEN/mTOR/STAT3 pathway in breast cancer stem-like cells is required for viability and maintenance. Proc Natl Acad Sci U S A 2007;104:16158–63.
39. Lee HE, Kim JH, Kim YJ, Choi SY, Kim SW, Kang E, et al. An increase in cancer stem cell population after primary systemic therapy is a poor prognostic factor in breast cancer. Br J Cancer 2011;104:1730–8.
40. Vicent S, Garayoa M, Lopez-Picazo JM, Lozano MD, Toledo G, Thunnissen FB, et al. Mitogen-activated protein kinase phosphatase-1 is overexpressed in non-small cell lung cancer and is an independent predictor of outcome in patients. Clin Cancer Res 2004;10:3639–49.
41. Vicent S, Lopez-Picazo JM, Toledo G, Lozano MD, Torre W, Garcia-Corchon C, et al. ERK1/2 is activated in non-small-cell lung cancer and associated with advanced tumours. Br J Cancer 2004;90: 1047–52.
42. Guo WF, Lin RX, Huang J, Zhou Z, Yang J, Guo GZ, et al. Identification of differentially expressed genes contributing to radioresistance in lung cancer cells using microarray analysis. Radiat Res 2005;164:27–35.
43. Janmaat ML, Rodriguez JA, Gallegos-Ruiz M, Kruyt FA, Giaccone G. Enhanced cytotoxicity induced by gefitinib and specific inhibitors of the Ras or phosphatidyl inositol-3 kinase pathways in non-small cell lung cancer cells. Int J Cancer 2006;118:209–14.
44. Tomko RP, Xu R, Philipson L. HCAR and MCAR: the human and mouse cellular receptors for subgroup C adenoviruses and group B coxsackieviruses. Proc Natl Acad Sci U S A 1997;94:3352–6.
45. Dan M, Chantler JK. A genetically engineered attenuated coxsackievirus B3 strain protects mice against lethal infection. J Virol 2005;79: 9285–95.
46. Errington F, Steele L, Prestwich R, Harrington KJ, Pandha HS, Vidal L, et al. Reovirus activates human dendritic cells to promote innate antitumor immunity. J Immunol 2008;180:6018–26.
47. Zhang Y, Chirmule N, Gao GP, Qian R, Croyle M, Joshi B, et al. Acute cytokine response to systemic adenoviral vectors in mice is mediated by dendritic cells and macrophages. Mol Ther 2001;3: 697–707.
48. Benencia F, Courreges MC, Conejo-Garcia JR, Mohamed-Hadley A, Zhang L, Buckanovich RJ, et al. HSV oncolytic therapy upregulates interferon-inducible chemokines and recruits immune effector cells in ovarian cancer. Mol Ther 2005;12:789–802.
49. Vicari AP, Chiodoni C, Vaure C, Ait-Yahia S, Dercamp C, Matsos F, et al. Reversal of tumor-induced dendritic cell paralysis by CpG immunostimulatory oligonucleotide and anti-interleukin 10 receptor antibody. J Exp Med 2002;196:541–9.
50. Pichlmair A, Reis e Sousa C. Innate recognition of viruses. Immunity 2007;27:370–83.
51. Jablonska J, Leschner S, Westphal K, Lienenklaus S, Weiss S. Neutrophils responsive to endogenous IFN-beta regulate tumor angiogenesis and growth in a mouse tumor model. J Clin Invest 2010;120: 1151–64.

OPEN ACCESS Freely available online

PLoS one

Intra-Aortic Clusters Undergo Endothelial to Hematopoietic Phenotypic Transition during Early Embryogenesis

Chiyo Mizuochi[1], Stuart T. Fraser[2], Katia Biasch[3], Yuka Horio[1], Yoshikane Kikushige[4], Kenzaburo Tani[5], Koichi Akashi[4], Manuela Tavian[3], Daisuke Sugiyama[1]*

1 Department of Hematopoietic Stem Cells,SSP Stem Cell Unit,Kyushu University Faculty of Medical Sciences, Fukuoka, Japan, **2** Laboratory of Blood Cell Development, Disciplines of Physiology, Anatomy and Histology, School of Medical Sciences, University of Sydney, Camperdown, New South Wales, Australia, **3** Unité 682 INSERM, Strasbourg, France, **4** Department of Medicine and Biosystemic Science, Kyushu University Graduate School of Medical Sciences, Fukuoka, Japan, **5** Department of Molecular Genetics, Medical Institute of Bioregulation, Kyushu University, Fukuoka, Japan

Abstract

Intra-aortic clusters (IACs) attach to floor of large arteries and are considered to have recently acquired hematopoietic stem cell (HSC)-potential in vertebrate early mid-gestation embryos. The formation and function of IACs is poorly understood. To address this issue, IACs were characterized by immunohistochemistry and flow cytometry in mouse embryos. Immunohistochemical analysis revealed that IACs simultaneously express the surface antigens CD31, CD34 and c-Kit. As embryos developed from 9.5 to 10.5 dpc, IACs up-regulate the hematopoietic markers CD41 and CD45 while down-regulating the endothelial surface antigen VE-cadherin/CD144, suggesting that IACs lose endothelial phenotype after 9.5 dpc. Analysis of the hematopoietic potential of IACs revealed a significant change in macrophage CFC activity from 9.5 to 10.5 dpc. To further characterize IACs, we isolated IACs based on CD45 expression. Correspondingly, the expression of hematopoietic transcription factors in the CD45(neg) fraction of IACs was significantly up-regulated. These results suggest that the transition from endothelial to hematopoietic phenotype of IACs occurs after 9.5 dpc.

Citation: Mizuochi C, Fraser ST, Biasch K, Horio Y, Kikushige Y, et al. (2012) Intra-Aortic Clusters Undergo Endothelial to Hematopoietic Phenotypic Transition during Early Embryogenesis. PLoS ONE 7(4): e35763. doi:10.1371/journal.pone.0035763

Editor: Alfons Navarro, University of Barcelona, Spain

Received March 3, 2011; **Accepted** March 22, 2012; **Published** April 27, 2012

Funding: This research was supported in part by the Project for Realization of Regenerative Medicine, Special Coordination Funds for Promoting Science and Technology of the Ministry of Education, Science, Sports and Culture (www.mext.go.jp/english); and SAKURA program of the Japan Society for the Promotion of Science (www.jsps.go.jp/english/index.html). The funders had no role in study design, data collection and analysis, decision to publish, or preparation of the manuscript.

Competing Interests: The authors have declared that no competing interests exist.

* E-mail: ds-mons@yb3.so-net.ne.jp

Introduction

During mouse embryogenesis, hematopoiesis begins at the extra-embryonic yolk sac (YS) at 7.5 days post-coitum (dpc) and shifts to fetal liver after mid-gestation, then to spleen and finally to bone marrow shortly before birth. There are two distinct waves of hematopoietic emergence: a transient wave, primarily restricted to erythropoiesis in YS blood islands prior to the connection of the circulation from the YS to the embryo; and a definitive wave originating in both the YS and embryo proper. The embryonic site has been identified in the aortic region, in the para-aortic splanchnopleura (p-Sp)/aorta-gonad-mesonephros (AGM) region [1–6]. Functional hematopoietic stem cells (HSCs) that can reconstitute adult recipients are first identified in the AGM region at 10.5 dpc after ex vivo organ culture [7]. The cells at 10.5 dpc that were not cultured ex vivo rarely reconstitute adult recipients, whereas those at 11.5 dpc can regardless [7–9]. Therefore, the cells that acquire HSC activity after culture step, have been termed "pre-HSC"s. Although several reports characterize the surface marker expression on both pre-HSCs at 10.5 dpc and HSCs at 11.5 dpc, the developmental process of HSC generation still remains unclear [8–11]. Cell populations capable of reconstituting neonatal recipients are detected in the p-Sp/AGM region at 9.5 dpc [12–13]. These observations suggest that ancestor cells of HSC from the p-Sp/AGM region at 9.5 dpc require special microenvironments to acquire HSC activity and that HSCs undergo phenotypic changes from 9.5 to 10.5 dpc. In the AGM region, intra-aortic/arterial clusters (IACs) are observed attached to floors of large arteries in several species including chicken, mouse and humans [3]. Mouse IACs have been characterized morphologically and are primarily located in three large arteries, namely, the dorsal aorta (DA), the omphalomesenteric (vitelline) artery (OMA; VA) and the umbilical artery (UA) [3,14–15]. IACs express both hematopoietic (CD41 and CD45) and endothelial (CD31, CD34 and VE-cadherin) surface markers [3,15–16] suggesting that IACs are likely equivalent to ancestor cells of HSC and/or pre-HSCs and are derived from endothelial cells (ECs) at aortic/arterial regions. Although recent genetic approaches and novel tracing methods demonstrate that IACs are derived from ECs in zebrafish and mice, it is unclear how IACs form and acquire HSC activity [17–25].

To address how IACs form and function in HSC generation, we first visualized IACs by immunohistochemistry and confocal imaging and were found to simultaneously express CD31, CD34 and c-Kit. This approach enabled us to investigate the phenotypic

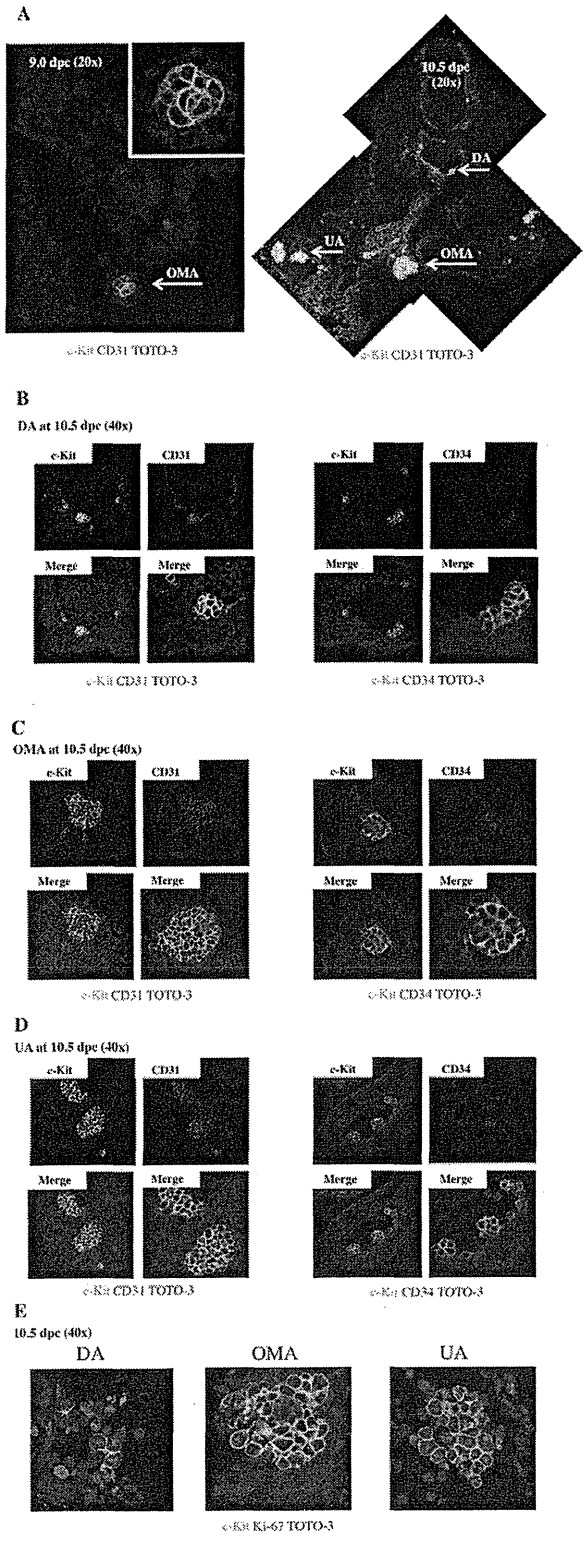

Figure 1. Confocal images of IACs expressing CD31/CD34/c-Kit in the AGM region. Transverse sections of AGM region from ICR mouse embryos at 9.0 and 10.5 dpc were stained with antibodies and observed by confocal microscopy. (**A**) IACs were observed in the omphalomesenteric artery (OMA) at 9.0 dpc (left; magnified view of IACs in upper right panel) and in the OMA, dorsal aorta (DA) and umbilical artery (UA) at 10.5 dpc (right). CD31 (red), c-Kit (green), and TOTO-3 (blue). Arrows indicate IACs. Original magnification is 20x. (**B-D**) IACs were observed in the DA (B), OMA (C) and UA (D) at 10.5 dpc. Left panel shows staining for CD31 (red), c-Kit (green), and TOTO-3 (blue), and right panel shows staining for CD34 (red), c-Kit (green), and TOTO-3 (blue) staining. Images were taken at 40x and zoom was used to show a detail at right lower panel. Another IAC in the DA is shown in Figure S1. (**E**) IACs expressing Ki-67, a marker of proliferation, were observed in the DA (left), OMA (middle) and UA (right). Ki-67 (red), c-Kit (green), and TOTO-3 (blue). Images were taken at 40x and zoom was used to show a detail.
doi:10.1371/journal.pone.0035763.g001

characterization of IACs by flow cytometry and hematopoiesis assays. Here, we demonstrate a significant transition from endothelial to hematopoietic cell phenotype of IAC cells after 9.5 dpc.

Results

Visualization of IACs in mouse embryos

Previous studies identified intra-aortic/arterial clusters (IACs) primarily by immunocytochemistry and microscopy [3,14–15]. Recently, we successfully visualized hematopoietic cell clusters in mouse placenta using thick (20 μm) cryo-sections and antibodies recognizing the embryonic HSC markers c-Kit, CD31 and CD34 and applied this method to quantifying IACs [26]. Cell aggregates consisting of more than three c-Kit-positive cells were defined as an IAC. Here, we used confocal microscopy to expand upon our previous study and characterize the cell types found within IACs according to c-Kit, CD31 and CD34 expression (Figure 1). The first IACs were observed as spherical structures in the omphalomesentric artery (OMA) at 9.0 dpc (12–14 somite pairs [SP]) (Figure 1A, left). Between 9.5 dpc (18–22 SP) to 10.5 dpc (30–34 SP), large arteries such as the dorsal aorta (DA), OMA and umbilical artery (UA) form [14]. IACs were observed in DA, OMA and UA at 10.5 dpc, and the size of IACs in the OMA and UA was significantly larger than those seen in the DA (Figure 1A, right). Localization of IACs in DA was not restricted to the ventral wall of DA, but rather some IACs were observed at dorsal and lateral sides of the wall (data not shown). All IACs in the DA, OMA and UA at 10.5 dpc simultaneously expressed c-Kit, CD31 and CD34 (Figure 1B-D). IACs expressing c-Kit in the different arteries analyzed were also positive for Ki-67, a marker of cell proliferation, regardless of location, suggesting that cells within IACs are highly proliferative (Figure 1E).

Characterization of IACs by flow cytometry and hematopoietic progenitor assays

To further characterize IACs, the caudal portion of embryos containing the p-Sp/AGM region was dissociated and analyzed by flow cytometry. At 10.5 dpc, c-Kit$^+$/CD31$^+$/CD34$^+$ cells, which are equivalent to IACs, were assessed for expression of the cell surface markers VE-cadherin/CD144 (an endothelial cell marker), CD41 (the earliest hematopoietic cell marker), CD45 (a pan-leukocyte marker), Sca-1 (a late fetal and adult HSC marker) and CD150 and EPCR (adult HSC markers) (Figure 2A-H). c-Kit$^+$/CD31$^+$/CD34$^+$ cells represented 0.069±0.01% in whole caudal portion of embryos. Among c-Kit$^+$/CD31$^+$/CD34$^+$ cells, VE-cadherin surface antigen expression decreased significantly within 24 hours from 9.5 to 10.5 dpc. Concomitantly, expression of the hematopoietic markers CD41 and CD45 increased from negative or low levels of expression on IAC cells at 9.5 dpc to abundant

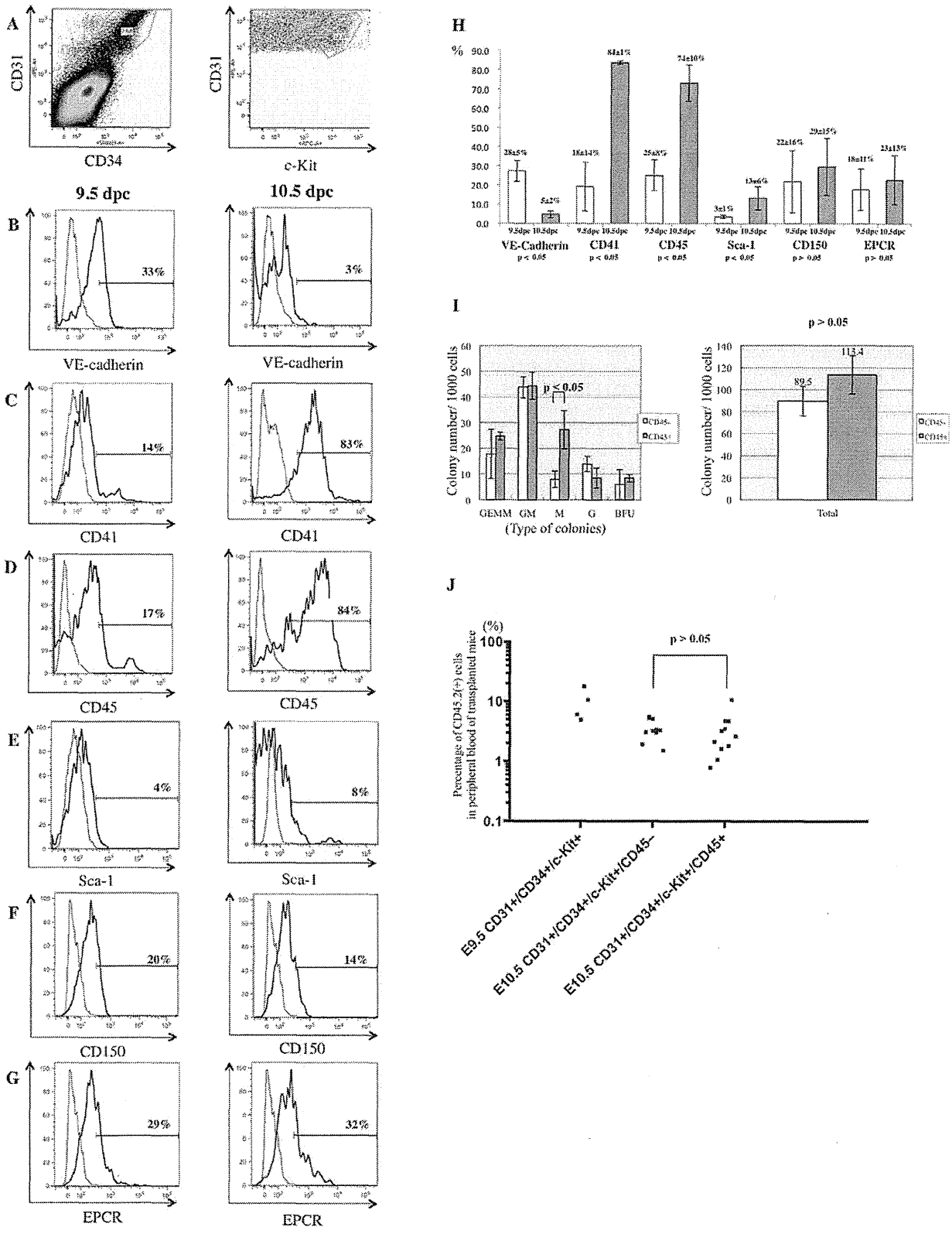

Figure 2. Flow cytometric analysis of CD31$^+$/CD34$^+$/c-Kit$^+$ AGM cells using surface expression of hematopoietic and endothelial cell markers. Single cell suspensions of the caudal portion of embryos containing the p-Sp/AGM region at 9.5 and 10.5 dpc were prepared and analyzed by flow cytometry. (**A**) Cells expressing CD31, CD34 and c-Kit markers of IACs were gated first. Isotype control of flow cytometric analysis is shown in

Figure S2. (**B-G**) Expression of hematopoietic and endothelial cell markers was analyzed on CD31$^+$/CD34$^+$/c-Kit$^+$ cells at 9.5 dpc (left) and 10.5 dpc (right) with the following antibodies: (**B**) VE-cadherin/CD144 (an endothelial cell marker), (**C**) CD41 (the earliest hematopoietic cell marker), (**D**) CD45 (a pan-leukocyte marker), (**E**) Sca-1 (a late fetal and adult HSC marker), (**F**) CD150 and (**G**) EPCR (adult HSC markers). At least 1,000 cells were assessed for each surface antigen. Representative profiles are shown. (**H**) Percentage of expression was summarized. At least 3 independent experiments were performed. Mean ± 2SD was calculated and shown at the top of bars. (**I**) One thousand sorted CD45-negative or CD45-positive CD31$^+$/CD34$^+$/c-Kit$^+$ cells were cultured in semisolid medium containing the hematopoietic cytokines, SCF (Stem Cell Factor), IL (Interleukin)-3, IL-6 and EPO (Erythropoietin). Left and right panels show each fraction and the total number of colonies, respectively. GEMM (colony-forming units of granulocyte erythrocyte monocyte macrophages); GM (of granulocyte macrophages); M (of macrophages); G (of granulocytes); BFU (burst forming units of erythroid cells). (**J**) 50–100 sorted CD31$^+$/CD34$^+$/c-Kit$^+$ cells at 9.5 dpc, as well as CD45-negative and CD45-positive CD31$^+$/CD34$^+$/c-Kit$^+$ cells were transplanted into busulfan-treated Ly5.1 mouse neonates. Approximately one year after transplantation, blood samples were collected and analyzed for CD45.2 expression by flow cytometry. Representative profile of flow cytometric analysis and its negative and positive controls are shown in Figure S3 and S6, respectively.
doi:10.1371/journal.pone.0035763.g002

levels at 10.5 dpc. Sca-1 expression also increased from 9.5 to 10.5 dpc.

We next separated c-Kit$^+$/CD31$^+$/CD34$^+$ cells based on CD45 expression by flow cytometry and performed colony assays and transplantation assays. As shown in Figure 2I (left), the number of CFU-M generated from CD45-positive c-Kit$^+$/CD31$^+$/CD34$^+$ cells (27.3) was significantly higher than CFU-M from CD45-negative c-Kit$^+$/CD31$^+$/CD34$^+$ cells (8.0) ($p<0.05$). However, the total number of hematopoietic colonies did not differ between CD45-negative and CD45-positive c-Kit$^+$/CD31$^+$/CD34$^+$ cells ($p>0.05$). When 50–100 c-Kit$^+$/CD31$^+$/CD34$^+$ cells were transplanted into neonate recipients, there was no significant difference in reconstitution ability (CD45-negative, 3.55%; CD45-positive 3.07%) ($p>0.05$) (Figure 2J). c-Kit$^+$/CD31$^+$/CD34$^+$ cells at 9.5 dpc were able to reconstitute recipients and chimerism to 9.89% was achieved. Presumptive ancestor cells of HSC can reportedly reconstitute neonate recipients but not adult recipients [13]. In addition, pre-HSCs at 10.5 dpc rarely reconstitute adult recipients without culture step [7–9,11]. When 100 c-Kit$^+$/CD31$^+$/CD34$^+$ cells were transplanted into adult recipients, no reconstitution was observed (data not shown).

Expression of CD45 in mouse and human intra-aortic/arterial clusters

CD45-negative and CD45-positive c-Kit$^+$/CD31$^+$/CD34$^+$ cells showed no difference in hematopoietic potential except within the macrophage lineage. To further investigate a role of CD45 expression on c-Kit$^+$/CD31$^+$/CD34$^+$ cells, we used flow cytometry to segregate c-Kit$^+$/CD31$^+$/CD34$^+$ cells into three fractions. Three distinct populations became apparent; CD45negative cells, CD45low cells, and CD45high cells (Figure 3A). The proportion of CD45-negative and CD45-low positive c-Kit$^+$/CD31$^+$/CD34$^+$ cells was higher at 9.5 dpc than at 10.5 dpc, whereas the percentage of CD45-high positive c-Kit$^+$/CD31$^+$/CD34$^+$ cells increased by 5-fold at 10.5 dpc (31.0%) compared to 9.5 dpc (6.3%) (Figure 3B). These data suggest that CD45-negative c-Kit$^+$/CD31$^+$/CD34$^+$ cells are precursors of CD45-high positive c-Kit$^+$/CD31$^+$/CD34$^+$ cells and that CD45 is a marker of IAC maturation. To address this issue, we examined expression levels of the gene encoding CD45 (*Ptprc; protein tyrosine phosphatase, receptor type, C*) and of various hematopoietic transcription factors (Runx1, c-Myb, Evi-1, SCL and Gata2) (Figure 3C-H). CD45-negative c-Kit$^+$/CD31$^+$/CD34$^+$ cells expressed low levels of *CD45* mRNA. *Ptprc* transcript levels increased significantly as CD45 surface protein expression was up-regulated in the c-Kit$^+$/CD31$^+$/CD34$^+$ population. Expression levels of all hematopoietic transcription factor genes assayed except *Evi-1* was highest in CD45-low positive c-Kit$^+$/CD31$^+$/CD34$^+$ cells. In agreement with flow cytometric analysis, evaluation of CD45 protein expression by immunohistochemistry indicated that IACs in the OMA at 9.5 dpc were CD45-negative while some IACs in the DA, OMA and UA were CD45-positive by 10.5 dpc (Figure 4A-D).

IAC formation in the developing human embryo is poorly defined. Having defined the developmental progression of IAC in the mouse above, we next examined IAC morphology and phenotype in a 32 day-old human embryo. Immunohistochemistry of embryonic human cryosections was performed using anti-human CD34 and CD45 antibodies. As shown in Figure 4E, IACs can be detected in ventral wall of the dorsal aorta. CD34 was expressed by a wide range of vascular endothelial cells throughout the embryo. CD45 was restricted to round and in many cases clearly circulating cells. However, within the IAC observable on the ventral wall of the dorsal aorta, cells expressing both CD34 and CD45 can be seen. This reflects the expression pattern we have identified in embryonic mouse IACs.

Transcription factor hierarchy in IAC development

We next observed IAC formation by immunohistochemistry and flow cytometry in mouse embryos harboring mutations associated with aberrant embryonic hematopoiesis [27–32]. Immunohistochemical analysis of *Runx1*$^{-/-}$ embryos lacked IACs in the DA, OMA and UA. Flow cytometric analyses confirmed the absence of c-Kit$^+$/CD31$^+$/CD34$^+$ cells in *Runx1*$^{-/-}$ embryos compared to wild type embryos (Figure 5A-B). *Evi-1*$^{-/-}$ embryos also lacked IACs in the DA, OMA and UA by immunohistochemistry. However, a small frequency of c-Kit$^+$/CD31$^+$/CD34$^+$ cells could be detected by flow cytometry (Figure 5C). In *c-Myb*$^{-/-}$ embryos, IACs were observed at the DA, OMA and UA, and c-Kit$^+$/CD31$^+$/CD34$^+$ cells were also observed by flow cytometry (Figure 5D). Collectively, these results demonstrate that Runx1 is essential for IAC formation while Evi-1 appears to be playing a function downstream of Runx1 in this process.

Discussion

During embryogenesis, a unique cell biological shift takes places in which endothelial cells with adherens junctions detach from each other, alter gene expression and become hematopoietic cells. This process is limited both anatomically and temporally. We here demonstrated that the transition from endothelial to hematopoietic phenotype of IACs occurs from 9.5 dpc in the mouse embryo, earlier than previously described. Furthermore, we show that IACs are identifiable in the human embryo based on CD45 expression, implying that this process in mice is applicable to human.

Previously, we reported an immunohistochemistry visualization technique revealing hematopoietic cell clusters in placenta using thick (20 μm) cryo-sections and antibodies recognizing embryonic HSC markers [26]. Here, we applied this technique to obtain high quality confocal images of intra-aortic/arterial clusters (IACs) in the AGM region. We defined IACs as c-Kit$^+$/CD31$^+$/CD34$^+$ cells. Recently, c-Kit$^+$/CD31$^+$/SSEA-1$^-$ cells were also identified in the AGM region [11]. As CD31 is expressed on both IACs and primordial germ cells (PGCs), it was necessary to exclude PGCs according to SSEA-1 expression. As shown in Figure 2 and 5, we

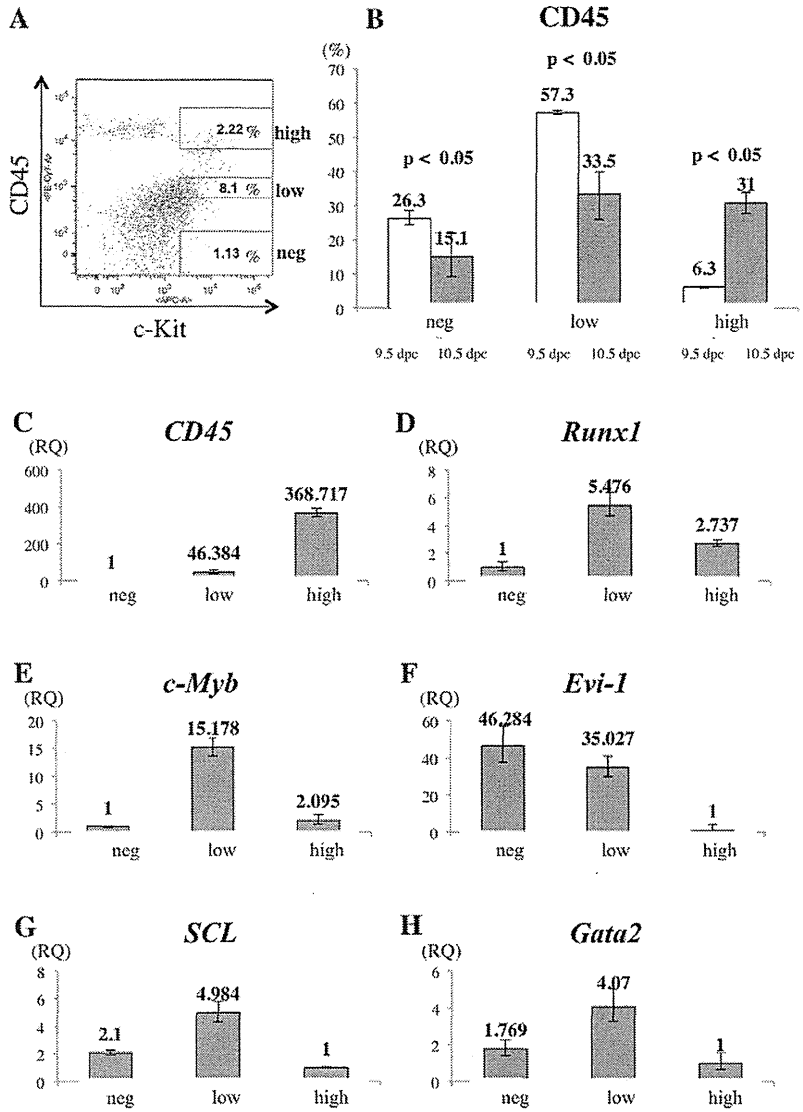

Figure 3. Gene expression analysis in CD31$^+$/CD34$^+$/c-Kit$^+$ AGM cells separated by CD45 expression. (**A**) Single cell suspensions of the caudal portion of embryos containing the AGM region at 10.5 dpc were prepared and analyzed by flow cytometry. Cells expressing CD31 and CD34, IAC markers, were first gated. The profile shows expression of c-Kit (x-axis) and CD45 (y-axis) in CD31$^+$/CD34$^+$ AGM cells (left). Based on intensity of CD45 expression, CD31$^+$/CD34$^+$/c-Kit$^+$ AGM cells were separated into three fractions, CD45-negative (under 10^2 of CD45-fluorescence, same as negative control), -low positive (from $10^{2.5}$ to $10^{3.5}$ of CD45-fluorescence), and -high positive (approximately over 10^4 of CD45-fluorescence). Isotype control and compensation samples of flow cytometric analysis are shown in Figure S4 and S5. (**B**) The percentage of CD45-negative, -low positive, and -high positive c-Kit$^+$/CD31$^+$/CD34$^+$ AGM cells was calculated both at 9.5 dpc (white bars) and 10.5 dpc (black bars). (**C-H**) Gene expression of *CD45* (C), *Runx1* (D), *c-Myb* (E), *Evi-1* (F), *SCL* (G) and *Gata2* (H) was analyzed in sorted CD45-negative, -low positive and -high positive c-Kit$^+$/CD31$^+$/CD34$^+$ AGM cells. Expression levels of *CD45* mRNA are up-regulated as c-Kit$^+$/CD31$^+$/CD34$^+$ cells express CD45 surface protein. Expression levels of *Runx1*, *c-Myb*, *Evi-1*, *SCL* and *Gata2* were highest in CD45-low positive c-Kit$^+$/CD31$^+$/CD34$^+$ cells, whereas that of *Evi-1* was highest in CD45-negative c-Kit$^+$/CD31$^+$/CD34$^+$ cells. RQ represents relative quantity of template in the original sample.
doi:10.1371/journal.pone.0035763.g003

could observe a small number of CD31$^+$/CD34$^-$ cells, which are likely to be PGCs. Since PGCs do not express CD34 at this stage, we could positively select the IAC fraction based on our definition by flow cytometry [33]. Our observation of IACs is compatible with the result showing large IACs were primarily observed in omphalomesentric artery (OMA) and umbilical artery (UA) at 10.5 dpc [11]. In the mouse, IACs protruding into the lumen of arteries were previously reported at 9.5 dpc in studies using microscopy and Tie-2 immunohistochemistry [14,34]. Prior to 9.5 dpc, we identified the first IACs, which formed a spherical structure, in the OMA at 9.0 dpc (Figure 1A). The OMA appears at 8.0 dpc and directly connects with the dorsal aorta (DA). The OMA anastomoses with the DA after 9.5 dpc and loses its connection with the UA by 10.5 dpc [14,35]. Our data (Figure 1E) indicate that IACs are proliferative, based on Ki-67 staining. Taken together, it is likely that the first IACs in the OMA proliferate and are distributed into

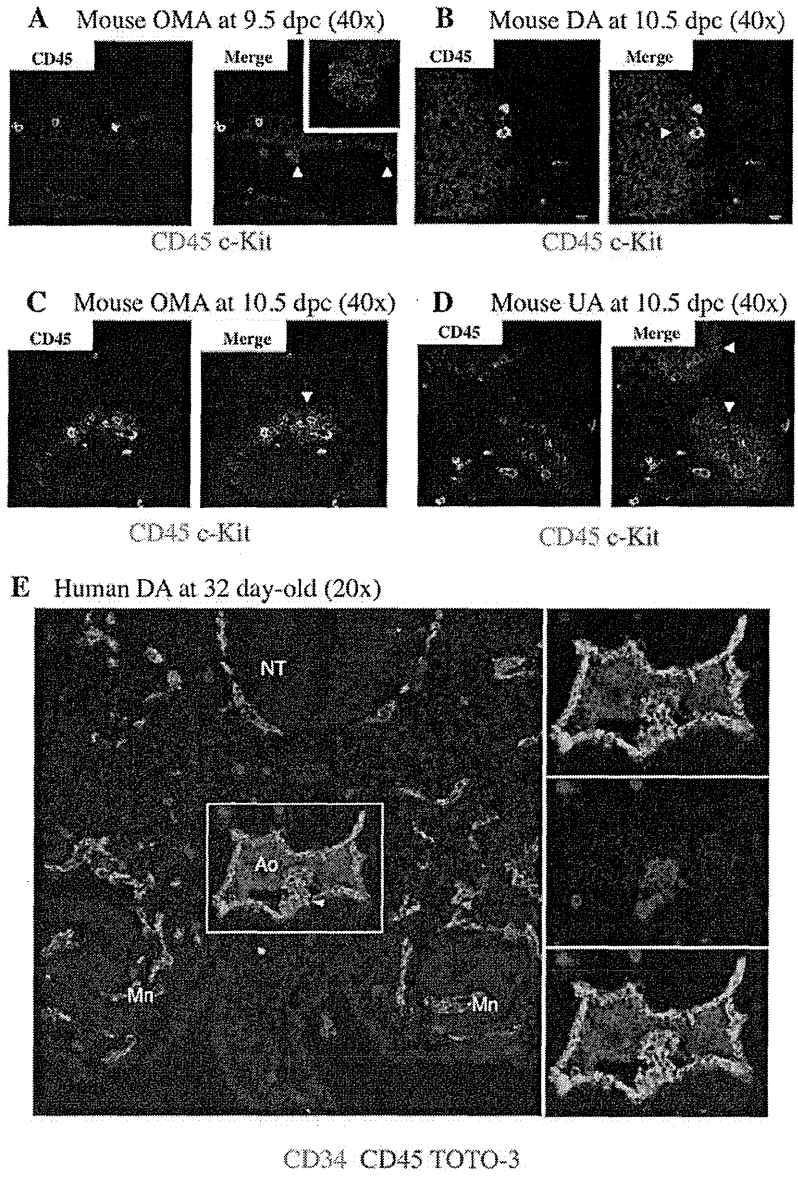

Figure 4. Expression of CD45 by mouse and human IACs. Transverse sections of AGM region were made from ICR mouse embryos at 9.5 and 10.5 dpc and from human embryos at 32 day-old, according to the Carnegie classification, stained with antibodies and observed by confocal microscopy. Arrowheads indicate IACs. (**A**) Mouse IACs in the omphalomesenteric artery (OMA) at 9.5 dpc expressed c-Kit, but not CD45. CD45 (green) and c-Kit (red). Magnified view of IACs is shown at right upper panel in Merge panel. Original magnification is 40x. (**B-D**) Mouse IACs in the dorsal aorta (DA) (B), OMA (C) and umbilical artery (UA) (D) at 10.5 dpc expressed c-Kit, and some expressed CD45. CD45 (green) and c-Kit (red). Original magnification is 40x. (**E**) All human IACs in the DA expressed CD34, and some expressed CD45. CD34 (green), CD45 (red) and TOTO-3 (blue). NT (Neural Tube); Ao (Aorta); Mn (Mesonephros). Original magnification is 20x.
doi:10.1371/journal.pone.0035763.g004

large arteries, such as the DA and UA, as the arterial system develops. Although several reports provide direct evidence that endothelial cells (ECs) generate IACs, we cannot rule out the possibility that either mesodermal cells, the ancestors of hematopoietic cells, or so-called hemangioblasts, which give rise both to ECs and hematopoietic cells, generate IACs by another pathway [17–25]. When VE-cadherin$^+$/CD45$^-$ cells were sorted out from AGM regions at 10.5 dpc, and co-aggregated with OP9 stromal cells, these cells acquired HSC activity [8]. As embryos develop, VE-cadherin$^+$/CD45$^+$ cells from AGM regions at 11.5 dpc can reconstitute adult recipients without culture step, whereas both VE-cadherin$^+$/CD45$^{+/-}$ cells can after aggregation culture with OP9 stromal cells. It suggests that the transition from endothelial to hematopoietic phenotype in pre-HSCs occurs between 10.5 and 11.5 dpc. According to our flow cytometric analysis of IACs, the transition from endothelial to hematopoietic phenotype occurs after 9.5 dpc (Figure 2). Although we found that 33% of c-Kit$^+$/CD31$^+$/CD34$^+$ cells at 9.5 dpc express VE-cadherin, most IACs defined as

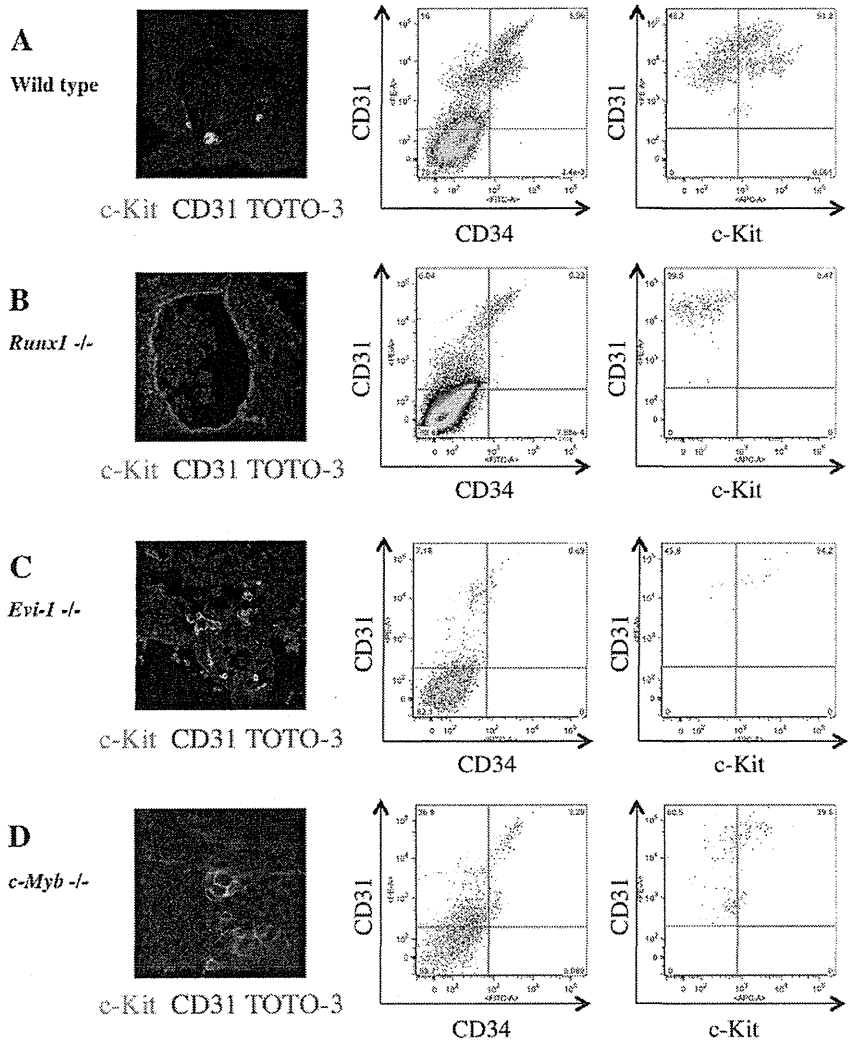

Figure 5. Altered IAC phenotype in *Runx1*$^{-/-}$, *Evi-1*$^{-/-}$ and *c-Myb*$^{-/-}$ embryos. Transverse sections of the AGM region were made from ICR, *Runx1*$^{-/-}$, *Evi-1*$^{-/-}$ and *c-Myb*$^{-/-}$ mouse embryos at 10.5 dpc, stained with antibodies and observed by confocal microscopy. Single cell suspensions of AGM regions from these embryos at 10.5 dpc were prepared and analyzed by flow cytometry. (**A-D**) Left panels show confocal images stained with anti-c-Kit (green) and CD31 (red) antibodies and TOTO-3 (blue). Middle and right panels show flow cytometric profiles of CD34 (x-axis) and CD31 (y-axis), and c-Kit (x-axis) and CD31 (y-axis), respectively. Isotype control and compensation samples of flow cytometric analysis are shown in Figure S2 and S5. (**A**) ICR mouse embryos serve as (wild type) controls. IACs and CD31$^+$/CD34$^+$/c-Kit$^+$ AGM cells were observed. (**B**) No IACs were observed in *Runx1*$^{-/-}$ embryos, whereas the aortic structure was conserved (left). No CD31$^+$/CD34$^+$/c-Kit$^+$ AGM cells were observed, whereas CD31$^+$/CD34$^+$/c-Kit$^-$ AGM cells, which are equivalent to ECs, were observed (middle and right). (**C**) No IACs were observed and aortic structure was altered in *Evi-1*$^{-/-}$ embryos (left). CD31$^+$ AGM cells were observed, but they did not express CD34 and c-Kit (middle and right). (**D**) IACs were observed in *c-Myb*$^{-/-}$ embryos and the aortic structure was conserved (left). CD31$^+$/CD34$^+$/c-Kit$^+$ AGM cells were observed (middle and right).
doi:10.1371/journal.pone.0035763.g005

c-Kit$^+$/CD31$^+$/CD34$^+$ cells by flow cytometry did not contribute to blood vessel structure. VE-cadherin is expressed in IACs as well as in ECs [16]. It is likely that sorted VE-cadherin$^+$/CD45$^-$ cells from AGM regions at 10.5 dpc contained ECs with HSC potential in addition to some IACs. Further studies are necessary to determine how ECs contribute to IAC generation. CD150 belongs to the SLAM family and its expression is developmentally regulated on the surface of HSCs. At 11.5 dpc, CD150$^-$ cells can reconstitute adult recipients, but CD150$^+$ cells not [10]. In this study, CD150 expression was examined on c-Kit$^+$/CD31$^+$/CD34$^+$ cells by flow cytometry and the percentage of CD150 expression was not changed (Figure 2F, H). It will be interesting to compare the CD150 expression between 10.5 and 11.5 dpc.

The pan-leukocyte marker CD45 is a transmembrane glycoprotein that functions as a protein phosphotyrosine phosphatase. Although loss of the *CD45* gene results in T and B lymphocyte anomalies in adult, there appears to be no significant abnormality in HSC development during embryogenesis [36–38]. We observed that CD45 protein expression was up-regulated in c-Kit$^+$/CD31$^+$/CD34$^+$ cells between 9.5 and 10.5 dpc (Figure 2D). Our results are compatible with the report showing that CD45 is expressed on the surface of IACs at 10.5 dpc, but not on the IACs at 9.5 dpc [11].

In agreement with previous reports, we observed no significant differences in HSC activity based on neonatal transplantation, whereas myeloid potential differs based on colony formation assay between CD45-negative and CD45-positive c-Kit$^+$/CD31$^+$/CD34$^+$ cells, suggesting that CD45 expression is not required for hematopoietic cell identity (Figure 2I, J) [39–40]. However, pre-HSCs that can reconstitute both adult and neonatal recipients appear at 10.5 dpc, whereas presumptive ancestor cells of HSC that can reconstitute only neonatal but not adult recipients appear at 9.5 dpc [7,12–13]. In accordance with flow cytometric data, some IACs expressed CD45 while others did not in both 10.5 dpc mouse embryos and 32 day-old human embryos (Figure 4B-E). Taken together, although CD45 does not function in HSC development, its expression on the cell surface might serve as a marker of pre-HSC maturation from ancestor cells of HSC. With regard to myeloid potential, only macrophage development differs (Figure 2I). At 10.5 dpc, macrophages are reportedly c-Kit$^-$/CD31$^-$/CD45$^+$ cells, and we could observe some c-Kit$^-$/CD45$^+$ cells in the AGM regions (Figure 4) [11]. CD45 expression on c-Kit$^+$/CD31$^+$/CD34$^+$ cells might be the diverging point of myeloid potential. Furthermore, we identified *CD45* gene expression in CD45-negative c-Kit$^+$/CD31$^+$/CD34$^+$ cells, suggesting that these cells are primed to differentiate into CD45-positive c-Kit$^+$/CD31$^+$/CD34$^+$ cells. Expression levels of *Runx1, c-Myb, SCL* and *Gata2* were highest in CD45-low positive c-Kit$^+$/CD31$^+$/CD34$^+$ cells, implying that the transition from endothelial to hematopoietic phenotype of IACs occurs in CD45-low positive c-Kit$^+$/CD31$^+$/CD34$^+$ cells, as these transcription factors are reportedly important for the switch to hematopoietic cells [22]. Evi-1 is involved in vasculo-angiogenesis in addition to HSC development [31]. Therefore, high expression level of *Evi-1* gene in CD45-negative c-Kit$^+$/CD31$^+$/CD34$^+$ cells implies that this population still preserves some endothelial identity.

We also investigated IACs from *Runx1*$^{-/-}$, *Evi-1*$^{-/-}$ or *c-Myb*$^{-/-}$ mouse embryos. Runx1 is essential for definitive hematopoiesis, and its expression marks the site of *de novo* generation of definitive hematopoietic cells [28–30]. In agreement with previous reports, we observed an absence of IACs in *Runx1*$^{-/-}$ mouse embryos. *Evi-1*$^{-/-}$ mouse embryos displayed abnormalities in vascular and hematopoietic development [31–32]. As shown in Figure 5C, *Evi-1*$^{-/-}$ mouse embryos comprised a few c-Kit$^+$/CD31$^+$/CD34$^+$ cells based on flow cytometric analysis. High expression of *Evi-1* in CD45-negative c-Kit$^+$/CD31$^+$/CD34$^+$ cells may correlate with vascular development and impairment of IAC formation. c-Myb is essential for HSC maturation and proliferation, and *c-Myb*$^{-/-}$ mouse embryos die at 15.5 dpc from impaired definitive hematopoiesis in fetal liver, although primitive hematopoiesis appears normal [27]. In contrast to *Runx1*$^{-/-}$ or *Evi-1*$^{-/-}$ mouse embryos, *c-Myb*$^{-/-}$ mouse embryos exhibited IACs.

Several evidences reveal that HSCs are generated from ECs [17–21]. Taken together, our results corroborate HSC-generation from ECs and imply that IACs gradually acquire hematopoietic phenotype after 9.5 dpc. Understanding how IACs are generated could lead to an understanding of how to manipulate HSC generation from ES/iPS cells and thus be applicable to future clinical applications.

Materials and Methods

Mice

Ly5.1 (Sankyo Labo Service, Tokyo, Japan) mice, Ly5.2 adult C57/BL6 mice (Kyudo, Tosu, Japan), ICR mice (SLC, Hamamatsu, Japan), *Runx1*$^{+/-}$ mice (provided by Dr. Speck at University of Pennsylvania), *Evi-1*$^{+/-}$ mice (JAX mice and Services, Bar Harbor, ME) and *c-Myb*$^{+/-}$ mice (JAX mice and Services) were used in these studies. To analyze cells, pregnant mice were sacrificed at 9.0–10.5 dpc and somite pair number was counted. Embryos at 9.0 dpc with 12–14 somite pairs (SP), 9.5 dpc with 18–22 SP and 10.5 dpc with 30–34 SP were dissected out, respectively. Animals were handled according to the Guidelines for the Care and Use of Laboratory Animals of Kyushu University. This study was approved by Animal Care and Use Committee, Kyushu University (Approval ID: A21-068-0).

Mouse immunohistochemistry

Embryos were dissected out and fixed in 2% paraformaldehyde in PBS, followed by equilibration in 30% sucrose in PBS. Embryos were embedded in OCT compound (SAKURA, Tokyo, Japan) and frozen in liquid nitrogen. Tissues were sliced at 20 μm on a Leica CM1900 UV cryostat, transferred to glass slides (Matsunami, Osaka, Japan) and dried thoroughly. Sections were blocked in 1% BSA in PBS and incubated in PBS containing 1% BSA with appropriate dilutions of the following primary antibodies: goat anti-mouse c-Kit (R&D Systems, Minneapolis, MN), rat anti-mouse CD31 (BD Biosciences, San Diego, CA), rat anti-mouse CD34 (BD Biosciences), rat anti-mouse CD45 (Biolegend) and rat anti-mouse Ki-67 antigen (Dako Corporation, Carpinteria, CA) at 4°C overnight. After washing in PBS three times, sections were incubated with appropriate dilutions of the following secondary antibodies: Alexa Fluor 488 donkey anti-rat IgG (Invitrogen, Carlsbad, CA), Alexa Fluor 488 donkey anti-goat IgG (Invitrogen), Alexa Fluor 546 donkey anti-goat IgG (Invitrogen) and Alexa Fluor 568 donkey anti-goat IgG (Invitrogen), as well as TOTO-3 (Invitrogen) to stain nuclei, at room temperature for 30 minutes. Samples were mounted on coverslips using fluorescent mounting medium (Dako Corporation) and assessed using a FluoView 1000 confocal microscope (Olympus, Tokyo, Japan).

Human tissues

Human embryos were obtained from voluntary abortions performed according to guidelines and with the approval of the French National Ethics Committee. In all cases, written consent allowing use of the embryo for research was obtained from the patient. Developmental age was estimated based on anatomical criteria and the Carnegie classification as previously described [41–42].

Human immunohistochemistry

Embryos were fixed overnight at 4°C in PBS plus 4% paraformaldehyde (Sigma-Aldrich), rinsed twice in PBS, then in PBS/15% sucrose (Sigma-Aldrich) for at least 24 hours. Tissues were then embedded in PBS with 15% sucrose and 7.5% gelatin (Sigma-Aldrich), frozen and stored at -80°C. Frozen sections (5 μm) were stored at −20°C until use, and then thawed and hydrated in PBS [37]. For double-staining, the TSA Plus Fluorescence amplification system was used, according to the manufacturer's instructions (NEN-Perkin Elmer). Endogenous peroxidases were inhibited for 20 minutes in PBS containing 0.2% hydrogen peroxide (Sigma-Aldrich). Sections were washed in PBS and non-specific binding sites were blocked with PBS/5% goat serum (Vector Laboratories) for 1 hour. Sections were then incubated with uncoupled antibody to CD45 (overnight at room temperature). After rinsing, sections were incubated with biotinylated goat anti-mouse IgG antibody (Immunotech) for 1 hour and then with peroxidase-labeled streptavidin (Immunotech) for 1 hour. Staining was revealed using fluorescent tyramide (TMR, Tetramethylrhodamine). Residual peroxidase activity was inhibited in PBS/0.2% hydrogen peroxide for 10 min at RT. After 3

washings in PBS, slides were treated with an Avidin/Biotin blocking kit according to the manufacturer's instructions (Vector Laboratories). Sections were washed and incubated with anti-CD34 antibody at room temperature for 2 hours, then with biotinylated goat anti-mouse IgG antibody (Immunotech) for 1 hour at RT, and with Alexa 488-labeled streptavidin for 1 hour. Slides were mounted in Vectashield medium (Vector Laboratories). Monoclonal antibodies to CD34 (IgG1, clone Qbend-10) and CD45 (IgG1, clone Hle-1) were purchased from Immunotech and Becton-Dickinson Biosciences, respectively.

Cell preparation

The caudal portion of embryos containing the p-Sp/AGM region was used to obtain a single cell suspension. Tissues were incubated with 1 mg/ml collagenase in medium supplemented with 10% fetal bovine serum for 30 minutes at 37°C and filtered through 40-μm nylon cell strainers (BD Biosciences).

Flow cytometry and cell sorting

Antibodies used for analysis were: FITC-conjugated anti-mouse CD41 (eBioscience, San Diego, CA), FITC-conjugated anti-mouse Sca-1 (eBioscience), FITC-conjugated anti-mouse EPCR (Endothelial Protein C Receptor) known as CD201 (Stem Cell Technologies inc, Vancouver, BC), PE-conjugated anti-mouse CD31 (BD Biosciences), PE-Cy7-conjugated anti-mouse CD45 (BioLegend), APC and APC-Cy7-conjugated anti-mouse c-Kit (BD Biosciences), Aexa Fluor488-conjugated anti-mouse CD150 (BioLegend), APC-conjugated anti-mouse VE-cadherin (clone name; VECD-1, provided by Dr. Ogawa at Kumamoto University), and FITC and Pacific Blue-conjugated anti-mouse CD34 (eBioscience). Flow cytometric analysis and cell sorting were carried out using a FACSAria SORP cell sorter (BDIS, San Jose, CA). Data files were analyzed using FlowJo software (Tree Star, Inc., San Carlos, CA).

RNA extraction and real-time PCR analysis

Total RNA was isolated using the RNAqueous 4PCR kit (Ambion Inc., Austin, Texas). mRNA was reverse transcribed using a High-Capacity RNA-to-cDNA kit (Life Technologies, Carlsbad, CA). The quality of cDNA synthesis was evaluated by amplifying mouse ß-actin using PCR. Thirty thermal cycles were used as follows: denaturation at 95°C for 10 sec, annealing at 60°C for 20 sec, followed by extension at 72°C for 20 seconds. Gene expression levels were measured by real time PCR with TaqMan® Gene Expression Master Mix and StepOnePlus™ real time PCR (Life Technologies). All probes were from TaqMan® Gene Expression Assays (Life Technologies). All analyses were performed in triplicate wells; mRNA levels were normalized to ß-actin and the relative quantity (RQ) of expression was compared with a reference sample.

Colony formation assay

Sorted cells were suspended in 3 ml of MethoCult® GF M3434 (Stemcell Technologies) distributed into three 35 mm dishes and then incubated in 5% CO_2 at 37°C. Colonies were counted up 14 days later using an inverted phase contrast microscope CKX41 (Olympus, Tokyo, Japan).

Transplantation assay

To examine neonatal repopulating HSCs, sorted cells were transplanted into busulfan-treated Ly5.1 mouse neonates as described previously [9,15]. Briefly, time-pregnant mice were injected on days 17 and 18 after conception with 15 μg of busulfan/gram body weight of the mother (Sigma-Aldrich, St.Louis MO). Isolated cells were suspended in 25 μl PBS and transplanted into neonates at the time of delivery using a 100 μl Hamilton syringe (Hamilton, Reno, NV). Approximately one year after transplantation, blood samples were collected, lysed in BD Pharm Lyse (BD Biosciences) and analyzed for CD45.2 expression by flow cytometry.

Supporting Information

Figure S1 Additional confocal images of IAC expressing CD31/CD34/c-Kit in the dorsal aorta of AGM region at 10.5 dpc. Staining for CD34 (red), c-Kit (green), and TOTO-3 (blue) is shown. Original magnification is 40x.
(TIFF)

Figure S2 Single cell suspensions of the caudal portion of embryos containing the p-Sp/AGM region at 9.5 and 10.5 dpc were prepared and analyzed by flow cytometry. Upper panels show isotype control of analysis corresponding to Figure 2A. Lower panels show isotype control of analysis corresponding to Figure 5.
(TIFF)

Figure S3 50–100 sorted $CD31^-/CD34^+/c\text{-}Kit^+$ cells at 9.5 dpc, as well as CD45-negative and CD45-positive $CD31^+/CD34^+/c\text{-}Kit^+$ cells were transplanted into busulfan-treated Ly5.1 mouse neonates. Approximately one year after transplantation, blood samples were collected, lysed in lysing solution and analyzed for CD45.2 expression by flow cytometry. Representative profile of flow cytometric analysis is shown.
(TIFF)

Figure S4 Single cell suspensions of the caudal portion of embryos containing the AGM region at 10.5 dpc were prepared and analyzed by flow cytometry. The profile shows isotype control of analysis corresponding to Figure 3A. Based on the isotype control, sorting gates are set into three fractions, CD45-negative (under 10^2 of CD45-fluorescence, same as negative control), -low positive (from $10^{2.5}$ to $10^{3.5}$ of CD45-fluorescence), and -high positive (approximately over 10^4 of CD45-fluorescence).
(TIFF)

Figure S5 Single cell suspensions of the caudal portion of embryos containing the p-Sp/AGM region at 9.5 and 10.5 dpc were prepared and analyzed by flow cytometry. Compensation samples of analysis corresponding to Figure 3A and 5 were shown.
(TIFF)

Figure S6 Negative and positive controls to transplantation analysis are shown corresponding to Figure S3. Peripheral blood samples were obtained from Ly5.1 adult mouse for negative control and Ly5.2 adult C57/BL6 mice for positive control, respectively.
(TIFF)

Acknowledgments

We thank the Research Support Center, the Graduate School of Medical Sciences, Kyushu University for technical support, Drs. K. Nakao and K. Kulkeaw for technical support, and Dr. Elise Lamar for critical reading of our manuscript.

Author Contributions

Conceived and designed the experiments: DS. Performed the experiments: CM KB YH YK MT DS. Analyzed the data: CM SF KB MT DS. Contributed reagents/materials/analysis tools: CM KB MT KT KA DS. Wrote the paper: CM SF DS.

References

1. Dzierzak E, Speck NA (2008) Of lineage and legacy: the development of mammalian hematopoietic stem cells. Nat Immunol 9: 129–136.
2. Mikkola HK, Orkin SH (2006) The journey of developing hematopoietic stem cells. Development 133: 3733–3744.
3. Godin I, Cumano A (2002) The hare and the tortoise: an embryonic haematopoietic race. Nat Rev Immunol 2: 593–604.
4. Dieterlen-Lievre F, Pouget C, Bollerot K, Jaffredo T (2006) Are intra-aortic hemopoietic cells derived from endothelial cells during ontogeny? Trends Cardiovasc Med 16: 128–139.
5. Jaffredo T, Bollerot K, Sugiyama D, Gautier R, Drevon C (2005) Tracing the hemangioblast during embryogenesis: developmental relationships between endothelial and hematopoietic cells. Int J Dev Biol 49: 269–277.
6. Sugiyama D, Tsuji K (2006) Definitive hematopoiesis from endothelial cells in the mouse embryo; a simple guide. Trends Cardiovasc Med 16: 45–49.
7. Medvinsky A, Dzierzak E (1996) Definitive hematopoiesis is autonomously initiated by the AGM region. Cell 86: 897–906.
8. Taoudi S, Gonneau C, Moore K, Sheridan JM, Blackburn CC, et al. (2008) Extensive hematopoietic stem cell generation in the AGM region via maturation of VE-cadherin+CD45+ pre-definitive HSCs. Cell Stem Cell 3: 99–108.
9. Rybtsov S, Sobiesiak M, Taoudi S, Souilhol C, Senserrich J, et al. (2011) Hierarchical organization and early hematopoietic specification of the developing HSC lineage in the AGM region. J Exp Med 208: 1305–1315.
10. McKinney-Freeman SL, Naveiras O, Yates F, Loewer S, Philitas M, et al. (2009) Surface antigen phenotypes of hematopoietic stem cells from embryos and murine embryonic stem cells. Blood 114: 268–278.
11. Yokomizo T, Dzierzak E (2010) Three-dimensional cartography of hematopoietic clusters in the vasculature of whole mouse embryos. Development 137: 3651–3661.
12. Kumano K, Chiba S, Kunisato A, Sata M, Saito T, et al. (2003) Notch1 but not Notch2 is essential for generating hematopoietic stem cells from endothelial cells. Immunity 18: 699–711.
13. Yoder MC, Hiatt K, Dutt P, Mukherjee P, Bodine DM, et al. (1997) Characterization of definitive lymphohematopoietic stem cells in the day 9 murine yolk sac. Immunity 7: 335–344.
14. Garcia-Porrero JA, Godin IE, Dieterlen-Lievre F (1995) Potential intraembryonic hemogenic sites at pre-liver stages in the mouse. Anat Embryol (Berl) 192: 425–435.
15. Garcia-Porrero JA, Manaia A, Jimeno J, Lasky LL, Dieterlen-Lievre F, et al. (1998) Antigenic profiles of endothelial and hemopoietic lineages in murine intraembryonic hemogenic sites. Dev Comp Immunol 22: 303–319.
16. Fraser ST, Ogawa M, Yokomizo T, Ito Y, Nishikawa S (2003) Putative intermediate precursor between hematogenic endothelial cells and blood cells in the developing embryo. Dev Growth Differ 45: 63–75.
17. Jaffredo T, Gautier R, Eichmann A, Dieterlen-Lievre F (1998) Intraaortic hemopoietic cells are derived from endothelial cells during ontogeny. Development 125: 4575–4583.
18. Sugiyama D, Ogawa M, Hirose I, Jaffredo T, Arai K, et al. (2003) Erythropoiesis from acetyl LDL incorporating endothelial cells at the preliver stage. Blood 101: 4733–4738.
19. Sugiyama D, Arai K, Tsuji K (2005) Definitive hematopoiesis from acetyl LDL incorporating endothelial cells in the mouse embryo. Stem Cells Dev 14: 687–696.
20. Bertrand JY, Giroux S, Golub R, Klaine M, Jalil A, et al. (2005) Characterization of purified intraembryonic hematopoietic stem cells as a tool to define their site of origin. Proc Natl Acad Sci U S A 102: 134–139.
21. Zovein AC, Hofmann JJ, Lynch M, French WJ, Turlo KA, et al. (2008) Fate tracing reveals the endothelial origin of hematopoietic stem cells. Cell Stem Cell 3: 625–636.
22. Chen MJ, Yokomizo T, Zeigler BM, Dzierzak E, Speck NA (2009) Runx1 is required for the endothelial to haematopoietic cell transition but not thereafter. Nature 457: 887–891.
23. Bertrand JY, Chi NC, Santoso B, Teng S, Stainier DY, et al. (2010) Haematopoietic stem cells derive directly from aortic endothelium during development. Nature 464: 108–111.
24. Kissa K, Herbomel P (2010) Blood stem cells emerge from aortic endothelium by a novel type of cell transition. Nature 464: 112–115.
25. Boisset JC, van Cappellen W, Andrieu-Soler C, Galjart N, Dzierzak E, et al. (2010) In vivo imaging of haematopoietic cells emerging from the mouse aortic endothelium. Nature 464: 116–120.
26. Sasaki T, Mizuochi C, Horio Y, Nakao K, Akashi K, et al. (2010) Regulation of hematopoietic cell clusters in the placental niche through SCF/Kit signaling in embryonic mouse. Development 137: 3941–3952.
27. Mucenski ML, McLain K, Kier AB, Swerdlow SH, Schreiner CM, et al. (1991) A functional c-myb gene is required for normal murine fetal hepatic hematopoiesis. Cell 65: 677–689.
28. Okuda T, van Deursen J, Hiebert SW, Grosveld G, Downing JR (1996) AML1, the target of multiple chromosomal translocations in human leukemia, is essential for normal fetal liver hematopoiesis. Cell 84: 321–330.
29. Wang Q, Stacy T, Binder M, Marin-Padilla M, Sharpe AH, et al. (1996) Disruption of the Cbfa2 gene causes necrosis and hemorrhaging in the central nervous system and blocks definitive hematopoiesis. Proc Natl Acad Sci U S A 93: 3444–3449.
30. North T, Gu TL, Stacy T, Wang Q, Howard L, et al. (1999) Cbfa2 is required for the formation of intra-aortic hematopoietic clusters. Development 126: 2563–2575.
31. Yuasa H, Oike Y, Iwama A, Nishikata I, Sugiyama D, et al. (2005) Oncogenic transcription factor Evi1 regulates hematopoietic stem cell proliferation through GATA-2 expression. EMBO J 24: 1976–1987.
32. Goyama S, Yamamoto G, Shimabe M, Sato T, Ichikawa M, et al. (2008) Evi-1 is a critical regulator for hematopoietic stem cells and transformed leukemic cells. Cell Stem Cell 3: 207–220.
33. Wood HB, May G, Healy L, Enver T, Morris-Kay GM (1997) CD34 expression patterns during early mouse development are related to modes of blood vessel formation and reveal additional sites of hematopoiesis. Blood 90: 2300–2311.
34. Takakura N, Huang XL, Naruse T, Hamaguchi I, Dumont DJ, et al. (1998) Critical role of the TIE2 endothelial cell receptor in the development of definitive hematopoiesis. Immunity 9: 677–686.
35. Theiler K (1972) The house mouse: development and normal stages from fertilization to 4 weeks of age. Springer, Berlin Heidelberg New York.
36. Kishihara K, Penninger J, Wallace VA, Kundig TM, Kawai K, et al. (1993) Normal B lymphocyte development but impaired T cell maturation in CD45-exon6 protein tyrosine phosphatase-deficient mice. Cell 74: 143–156.
37. Byth KF, Conroy LA, Howlett S, Smith AJ, May J, et al. (1996) CD45-null transgenic mice reveal a positive regulatory role for CD45 in early thymocyte development, in the selection of CD4+CD8+ thymocytes, and B cell maturation. J Exp Med 183: 1707–1718.
38. Mee PJ, Turner M, Basson MA, Costello PS, Zamoyska R, et al. (1999) Greatly reduced efficiency of both positive and negative selection of thymocytes in CD45 tyrosine phosphatase-deficient mice. Eur J Immunol 29: 2923–2933.
39. North TE, de Bruijn MF, Stacy T, Talebian L, Lind E, et al. (2002) Runx1 expression marks long-term repopulating hematopoietic stem cells in the midgestation mouse embryo. Immunity 16: 661–672.
40. Matsubara A, Iwama A, Yamazaki S, Furuta C, Hirasawa R, et al. (2005) Endomucin, a CD34-like sialomucin, marks hematopoietic stem cells throughout development. J Exp Med 202: 1483–1492.
41. O'Rahilly R, Muller F (1987) Development Stages in Human Embryos. Washington: Carnegie Institution of Washington.
42. Tavian M, Peault B (2005) The changing cellular environments of hematopoiesis in human development in utero. Exp Hematol 33: 1062–1069.

Open Journal of Blood Diseases, 2012, 2, 1-10
doi:10.4236/ojbd.2012.21001 Published Online March 2012 (http://www.SciRP.org/journal/ojbd)

Scientific Research

Leukemogenic Fusion Gene (p190 BCR-ABL) Transduction into Hematopoietic Stem/Progenitor Cells in the Common Marmoset

Yan Dong[1], Seiichiro Kobayashi[1], Yamin Tian[1,2], Manabu Ozawa[1,2], Takafumi Hiramoto[2], Kiyoko Izawa[1], Yuansong Bai[1], Yasushi Soda[1], Erika Sasaki[3], Toshio Itoh[3], Yoshiro Maru[4], Satoshi Takahashi[1], Kaoru Uchimaru[5], Naoki Oyaizu[6], Arinobu Tojo[1], Chieko Kai[7], Kenzaburo Tani[2*]

[1]Division of Molecular Therapy, Institute of Medical Science, The University of Tokyo, Tokyo, Japan; [2]Department of Molecular Genetics, Medical Institute of Bioregulation, Kyushu University, Fukuoka, Japan; [3]Central Institute for Experimental Animals, Kawasaki, Japan; [4]Department of Pharmacology, Tokyo Woman's Medical University, Tokyo, Japan; [5]Department of Hematology/Oncology, Research Hospital, Institute of Medical Science, The University of Tokyo, Tokyo, Japan; [6]Department of Laboratory Medicine, Research Hospital, Institute of Medical Science, The University of Tokyo, Tokyo, Japan; [7]Laboratory Animal Research Center, Institute of Medical Science, The University of Tokyo, Tokyo, Japan.
Email: *taniken@bioreg.kyushu-u.ac.jp

Received December 9th, 2011; revised January 24th, 2012; accepted February 16th, 2012

ABSTRACT

Patients with Philadelphia chromosome (p190 BCR-ABL fusion gene)-positive acute lymphoblastic leukemia have a poor prognosis despite intensive therapeutic intervention. In this study, we attempted to develop a leukemia nonhuman primate model that mimics various human systems. Hematopoietic stem/progenitor cells in the common marmoset were transduced with a lentiviral vector containing the p190 BCR-ABL fusion gene by *ex vivo* transduction or *in vivo* direct bone marrow injection. In the latter model, BCR-ABL gene expression was maintained for more than one and a half years. One marmoset unexpectedly developed myelofibrosis-like disease. However, none of the marmosets have developed leukemia to date. In conclusion, we successfully achieved sustained p190 BCR-ABL gene expression *in vivo*. However, a genetic mutation in addition to p190 BCR-ABL may be required for the malignant transformation of hematopoietic stem/progenitor cells in the common marmoset during the short observation period. This novel *in vivo* approach will help develop a marmoset leukemia model in the future.

Keywords: Leukemia; Lentiviral Vector; Myelofibrosis; Common Marmoset

1. Introduction

Many preclinical *in vivo* studies have been conducted in mice because they are easy to breed and their biology and genetics are well-characterized. However, humans and mice differ genetically, pathophysiologically and pharmacokinetically, which makes it difficult to extrapolate the results from mouse models for direct clinical applications in humans. Large animals, especially nonhuman primates, are more closely related to humans. Moreover, because of their long life span, nonhuman primates can be treated and monitored over a long period, which presents opportunities for time-varying sampling of their blood and bone marrow. Thus, the development of non-human primate models that mimic human pathophysiology and pharmacokinetics will significantly further our understanding of human diseases. Particularly, genetically modified primates will be a powerful human disease model that can be used to preclinically assess the safety and efficacy of developing drugs.

Currently, Old World primates, such as the rhesus monkey (*Macaca mulatta*) and cynomolgus monkey (*Macaca fascicularis*), are commonly used for research [1-3]. However, these primates have several disadvantages, such as a slow sexual maturation period of approximately three years, fewer offspring over the female lifespan, and difficulty in handling.

The common marmoset (*Callithrix jacchus*) is a small New World primate that has attracted considerable attention as a potential animal for biomedical research [4,5]. The common marmoset is small, weighing approximately 350 - 400 g, relatively easy to breed, has a short gestation period of approximately 144 days, reaches sexual maturity at 12 - 18 months, and produces 40 - 80 offspring during the female lifespan. Thus, although marmosets are

*Corresponding author.

not as closely related to humans as apes or Old World primates, they are valuable as a potential primate model of human disease.

In this study, we attempted to establish a marmoset leukemia model by introducing a fusion gene that causes leukemia in humans. The Philadelphia chromosome (Ph) contains one of several forms of BCR and c-ABL gene fusions, and these fusions substantially contribute to the pathogenesis of chronic myelogenous leukemia (CML) and acute lymphoblastic leukemia (ALL). The p190 BCR-ABL fusion gene, in which BCR exon 1 is joined to ABL exon 2 (e1a2) and produces the p190 protein, is detected in 20% - 35% of ALL patients, and the prognosis of these patients is particularly poor [6,7]. Several treatments, such as allogeneic hematopoietic stem cell transplantation and novel small molecules that directly target the p190 BCR-ABL fusion gene have been developed to treat this refractory disease [8]. Transduction of the p190 BCR-ABL fusion gene is reportedly sufficient to cause leukemia in mice [9-11]. However, to date, there are no reports of a primate leukemia model. Establishing a marmoset model of this disease will be useful to test the efficacy of current and future treatments. Therefore, we transduced the p190 BCR-ABL fusion gene into marmoset $CD34^+$ hematopoietic stem/progenitor cells using a lentiviral vector and examined the occurrence of leukemogenic events.

2. Materials and Methods

2.1. Cell Lines

Ba/F3 cells, a mouse interleukin-3 (mIL-3)-dependent hematopoietic cell line, were maintained in RPMI (Invitrogen, Carlsbad, CA, USA) supplemented with 10% fetal bovine serum (FBS) and mIL-3 (10 ng/mL) at 37°C in 5% CO_2 and passaged twice every week.

2.2. Animals and Preparation of Bone Marrow and Peripheral Blood Mononuclear Cells

Common marmosets were purchased from the Division of Animal Experimentation, Central Institute for Experimental Animals (Kawasaki, Japan), and bred at the animal center at our institute. In this study five animals were used including one control marmoset. No. 591 (male, 2 years and 6 months old) and No. 2338 (female, 4 years and 9 months old) were used as *ex vivo* BCR-ABL transduction models. No. 2129 (female, 5 years and 7 months old) and No. 2223 (female, 5 years and 3 months old) were used as BCR-ABL direct *in vivo* injection models. The study protocol was approved by the animal ethical committee of the University of Tokyo.

Bone marrow samples were collected by flushing the femurs of euthanized animals or aspirating the femoral bone marrow with an aspiration needle (Task, Tochigi, Japan). Peripheral blood samples were collected with heparin. Mononuclear cells (MNCs) in each sample were isolated by density-gradient centrifugation with Lymphoprep (Axis-Shield, Oslo, Norway). The cells were frozen in liquid nitrogen until further use.

2.3. Construction, Production and Transduction of Lentiviral Vector

Third generation, VSV.G pseudotyped lentiviral vectors were produced by transiently cotransfecting four plasmids into 293T cells as previously described [12]. Briefly, the p190 BCR-ABL fusion gene driven by a CMV or PGK promoter (HIV-CMV/PGK-BCR-ABL) was inserted into the transfer vector [13]. This plasmid was cotransfected into 293T cells using the calcium-phosphate method. The viral supernatant was harvested 48 and 72 hrs post transfection. The viral pellet was collected by ultra-centrifuging the supernatant and then stored at –80°C. The DNA titer, which is known to reflect the amount of transducible vector genome, was determined by real-time quantitative PCR as previously described [14]. For transduction, a cell pellet (2×10^5) was mixed and incubated with concentrated viral supernatant (20 μL) for 2 hrs in a 37°C incubator. The cells were generally infected *in vitro* with an MOI (multiplicity of infection) of 2.

2.4. Detection of p190 BCR-ABL Transgene Expression

RNA extraction and reverse transcription were performed as previously described using an RNA/DNA extraction kit (Qiagen, Hilden, Germany) and SuperScript First-Strand Synthesis System for RT-PCR (Invitrogen). Nested PCR amplification of p190 BCR-ABL was performed using a GeneAmp PCR System 9700 (Applied Biosystems, Foster City, CA, USA) with primers that specifically amplify the e1a2 transcripts. A 50 μL reaction mixture containing 2 mM of each dNTP, 25 mM $MgCl_2$, 10× PCR buffer, 0.5 μM primers, 1.25 U AmpliTaq Gold (Applied Biosystems) and 10 ng cDNA was subjected to 40 cycles of denaturation (95°C, 30 sec), annealing (61°C, 30 sec), and extension (72°C, 30 sec) and another 40 cycles with the inner primer set of denaturation (95°C, 30 sec), annealing (57°C, 30 sec), and extension (72°C, 30 sec). The final products were analyzed on a 1% agarose gel stained with ethidium bromide. The outer BCR-ABL primer set was forward primer (5'-CGC TCT CCC TCG CAG AAC TC-3') and reverse primer (5'-GGA GTG TTT CTC CAG ACT GTT GAC TG-3'), while the inner primer set was forward primer (5'-AAC AGT CCT TCG ACA GCA GCA-3') and reverse primer (5'-GCG TGA TGT AGT TGC TTG GGA-

